






RESEARCH ARTICLE

Automated identification of occluded sectors in midlatitude cyclones: Method and some climatological applications

Catherine M. Naud¹  | Jonathan E. Martin²  | Poushali Ghosh²  |
Gregory Elsaesser¹  | Derek Posselt³ 

¹Columbia University/NASA-GISS,
New York, New York, USA

²University of Wisconsin-Madison,
Madison, Wisconsin, USA

³Jet Propulsion Laboratory, California
Institute of Technology, Pasadena,
California, USA

Correspondence

Jonathan E. Martin, University of
Wisconsin-Madison, Madison, WI, USA.
Email: jemarti1@wisc.edu

Funding information

National Aeronautics and Space
Administration, Grant/Award Numbers:
80NSSC20K0085, 80NM0018D0004

Abstract

A novel automated scheme for identifying occluded mid-latitude cyclones from gridded datasets is described and employed to construct a limited climatology of such storms as well as composites of their thermodynamic and kinematic structures. The climatology (2006–2017) is derived from the MERRA-2 reanalysis and reveals differences in the distribution of occlusions between the hemispheres. Northern Hemisphere occlusions are most frequent in winter (DJF) and are found poleward of the mean tropopause-level jets in both the Atlantic and Pacific basins. In the Southern Hemisphere, however, occlusions are most frequent during autumn (MAM) and are almost never found equatorward of 40°S. Using the identification scheme, wintertime occlusions are stratified based upon the value of 700 hPa θ_e (equivalent potential temperature) in their characteristic thickness ridges. Composites of six groups of occlusions, based upon this distinction, are constructed for each hemisphere. The composites reveal notable differences in the thermodynamic structures among these six groups with more poleward (lower θ_e or “colder”) storms exhibiting shallower, less developed thermal structures as compared to their lower-latitude (higher θ_e or “warmer”) counterparts. These differences are attended by contrasts in the intensity of upward vertical motions in the occluded sectors of the various composite storms implying that “warm” storms are associated with greater latent heat release than “colder” storms. It is suggested that these coincident differences between “cold” and “warm” storms provide further evidence of the fundamental importance of latent heat release to the development of occluded thermal structures.

KEYWORDS

automated identification, occlusion, thermal ridge, TROWAL

This is an open access article under the terms of the [Creative Commons Attribution-NonCommercial-NoDerivs](https://creativecommons.org/licenses/by-nc-nd/4.0/) License, which permits use and distribution in any medium, provided the original work is properly cited, the use is non-commercial and no modifications or adaptations are made.

© 2023 The Authors. *Quarterly Journal of the Royal Meteorological Society* published by John Wiley & Sons Ltd on behalf of the Royal Meteorological Society.

1 | INTRODUCTION

In their conceptual model of the mid-latitude cyclone, Bjerknes and Solberg (1922) were the first to suggest a relationship between the three-dimensional (3D) thermal structure of the storm and its associated distribution of clouds and precipitation. The model, which has come to be known as the Norwegian Cyclone Model (NCM), described how the amplification of the nascent cyclone distorted the polar front, the globe-girdling boundary separating polar air to the north from the tropical air to the south into the cold and warm fronts of the storm structure. The so-called warm sector, a region of homogeneously warm air between the two fronts, extended downward to the surface. The thermal evolution of such cyclones involves changes in both the vigor of the individual frontal zones and in their orientation with respect to one another. The dynamical processes that control this evolution are also responsible for producing the secondary circulations to which the characteristic cloud and precipitation distribution in cyclones – linear bands of varying widths along the cold and warm fronts and a cloud head poleward and westward of the storm center – can be accurately attributed.

Namias (1939) was among the first to examine the 3D airflow through cyclones and relate it to the attendant distribution of clouds and precipitation. He identified an ascending airstream, originating in the warm-sector boundary layer, that bifurcated into two separate streams – one turning cyclonically to the west and the other turning anticyclonically to the east. More recent studies by Browning and Harrold (1969), Harrold (1973), Carlson (1980), Young *et al.* (1987) and Browning (1990) have christened the latter as the warm conveyor belt. This feature has garnered considerable research attention in the ensuing 30 years (e.g., Berman and Torn, 2019; Eckhardt *et al.*, 2004; Madonna *et al.*, 2014; Martínez-Alvarado *et al.*, 2014; Schäfler and Harnisch, 2015; Wernli and Davies, 1997; Wernli, 1997). The cyclonically turning airstream has also been noted by Atkinson and Smithson (1974) as well as Iskenderian (1988), Kurz (1988), Mass and Schultz (1993), Schultz and Mass (1993) and Reed *et al.* (1994).

A notable element of the post-mature phase of the cyclone life cycle, with a bearing on these various airstreams, is the process of occlusion first conceived by Tor Bergeron (Jewell, 1981). Among the structural changes that characterize the occluded stage are the adoption of an increasingly equivalent barotropic structure in the vertical as well as the development of a lower-tropospheric thermal ridge connecting the sea-level pressure (SLP) minimum to the peak of the warm sector (Saucier, 1955; Wallace and Hobbs, 1977; Schultz and Mass, 1993; Martin, 1998a, 1998b; Martin, 1999a, 1999b; Posselt and Martin, 2004;

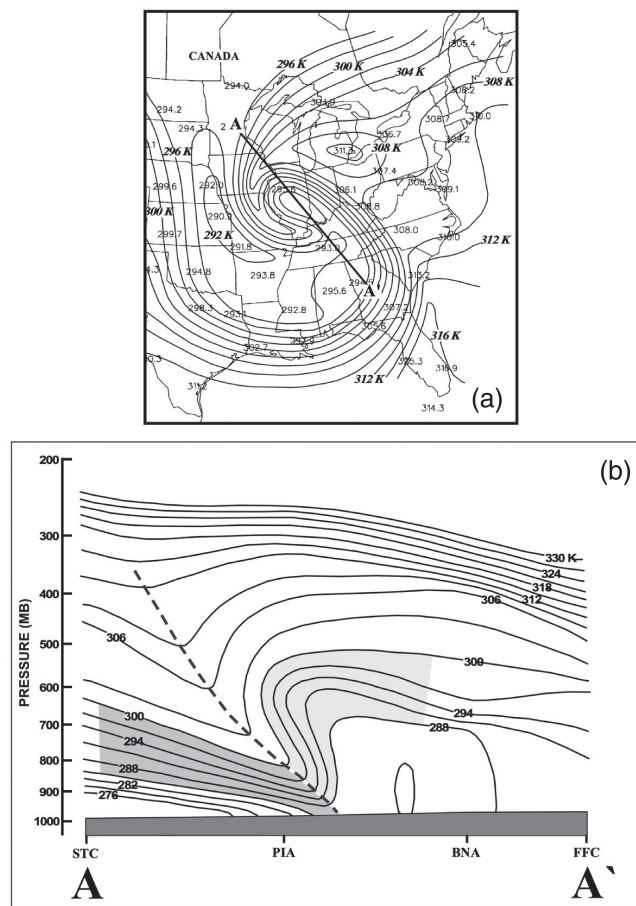


FIGURE 1 (a) Analysis of 700 hPa equivalent potential temperature (θ_e) observations at 0000 UTC 20 January 1995. θ_e labeled in K and contoured every 2 K. Cross-section along line A–A' shown in Figure 1b. (b) Vertical cross-section of equivalent potential temperature (θ_e) along line A–A' in Figure 1a (from St. Cloud MN [STC], to Peoria, IL [PIA], to Nashville, TN [BNA] to Peachtree City, GA [FFC]) at 0000 UTC 20 January 1995. Solid lines are moist isentropes labeled in K and contoured every 3 K. Dashed line indicates the canonical axis of maximum θ_e that slopes upward and poleward in a warm occlusion. Light (dark) shading represents the cold (warm)-frontal baroclinic zone involved in this occluded structure. Adapted from Martin (1998a)

Schultz and Vaughan, 2011). According to the NCM, the air occupying the thermal ridge originated in the surface warm sector and was forced to ascend by the intersection of the cold and warm fronts as the cyclone occludes. The resulting structure consists of an axis of maximum potential (θ) or equivalent potential (θ_e) temperature, in both horizontal and vertical cross-sections, embedded within a region of reduced static stability between two significant baroclinic zones, as depicted in Figure 1. Despite the sometimes fierce debate regarding the mechanisms that might operate to produce it (e.g., Schultz and Mass, 1993; Stoelinga *et al.*, 2002; Schultz and Vaughan, 2011), there is little disagreement that such a configuration represents the canonical thermal structure of a warm-occluded cyclone.

A more fully 3D representation of the warm-occluded thermal structure was developed in a series of papers over the course of more than a decade by scientists at the Canadian Meteorological Service (Crocker *et al.*, 1947; Godson, 1951; Penner, 1955; Galloway, 1958, 1960). These studies noted the ubiquity of a westward slope to the crests of the thermal wave at successive heights in occluded cyclones. Penner (1955) referred to this “sloping valley of tropical air,” as it had been previously described by Godson (1951), as the TROWAL (TROUgh of Warm air ALoft). Borrowing terminology from the NCM, the TROWAL essentially marks the 3D sloping intersection of the upper cold-frontal portion of the warm occlusion with the warm-frontal zone. The observation that the cloudiness and precipitation characteristic of the occluded sector of the cyclone bore a closer correspondence to the TROWAL position than to the weak surface warm-occluded front led the Canadians to regard the TROWAL as the essential structural feature of a warm-occluded cyclone. Consistent with the definition given by Penner (1955) and the description given by Godson (1951), the TROWAL can be approximately located either as a ridge of high θ , θ_e or 1,000:500 hPa thickness on a horizontal cross-section, and more precisely as a 3D sloping canyon in an isosurface of θ_e as shown in Martin (1998a, 1999a). In fact, unlike cold- and warm-frontal analyses that are drawn as lines on a single isobaric or geometric height surface, because occlusions are so strongly tied to the position of the sloping TROWAL, identifying them is inherently a 3D problem. A schematic illustrating the TROWAL conceptual model is given in Figure 2.

Compelling evidence supporting these earlier observational findings comes from a number of more recent fine-scale numerical modeling studies of occluded cyclones (Schultz and Mass, 1993; Reed *et al.*, 1994; Martin, 1998a, 1998b) that have illustrated the structure and thermal evolution of, and airflow through, the occluded sector. These studies have identified a coherent airstream, originating in the warm-sector boundary layer, that ascends cyclonically in the occluded sector of the cyclone. Martin (1998b, 1999a), noting a spatial relationship between the path taken by this airstream and the TROWAL in his case, referred to this airflow as the “TROWAL airstream.” By considering the insightful along- and across-isentrope partition of the Hoskins *et al.* (1978) Q vector first described by Keyser *et al.* (1992), Martin (1999a, 1999b) provided a dynamical explanation of the relationship between the development of the characteristic thermal structure in the occluded sector of cyclones and the associated ascent that supports this airstream. Consistent with forced ascent in a nearly saturated environment, the developing occluded thermal ridge is often associated with substantial latent-heat release (LHR).

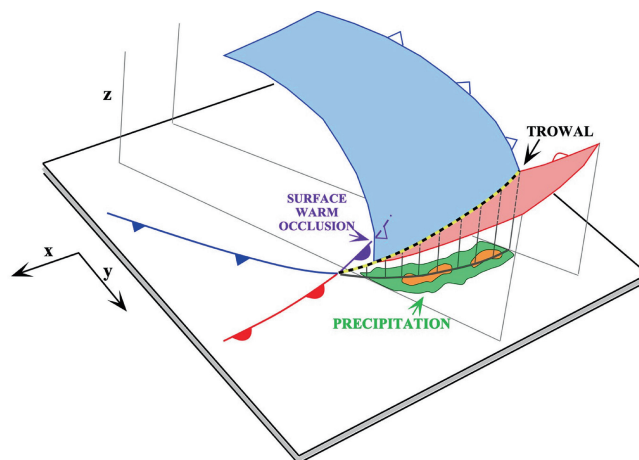


FIGURE 2 Schematic illustration of the TROWAL (TROUgh of Warm air ALoft) conceptual model. The blue-shaded surface represents the warm edge of the cold-frontal baroclinic zone. The pink-shaded surface represents the warm edge of the warm-frontal baroclinic zone. The thick dashed line (marked “TROWAL”) represents the three-dimensional sloping intersection between the cold- and warm-frontal zones characteristic of warm occlusions. Schematic precipitation band is indicated, as are the positions of the surface warm, cold, and occluded fronts. Dark solid line through the precipitation band represents the projection of the TROWAL to the surface. From Martin (1999a)

Martin (1998a) noted that some occluded cyclones are associated with a characteristic tropopause-level potential vorticity (PV) structure consisting of an isolated, low-latitude high-PV feature that is connected to a high-latitude reservoir of high PV by a thin filament of high PV – a structure he termed the “treble clef” (Figure 3). Given the relationship between tropopause-level PV and the thermal structure in the underlying troposphere (Hoskins *et al.*, 1985), the horizontal juxtaposition of two upper-level positive PV anomalies of unequal magnitude, separated by a relative minimum in PV (such as along line A–A’ in Figure 3a) depicts the canonical warm-occluded thermal structure (Figure 3b). From the perspective of the NCM, the sloping warm column beneath the upper-tropospheric PV minimum in Figure 3b represents warm-sector boundary-layer air that has been lifted during the occlusion process. In three dimensions, the warm axis identifies the position of the TROWAL which, as mentioned earlier, tends to be a focus for precipitation production in the occluded sector of cyclones. Thus, the clouds and precipitation in that portion of the storm are often nearly coincident with an upper-tropospheric PV minimum. The strong connection between the morphology of the upper-tropospheric PV and the underlying occluded thermal structure, coupled with the known diabatic influence on vertical PV redistribution (e.g., Eliassen and Kleinschmidt, 1957; Hoskins *et al.*, 1985;

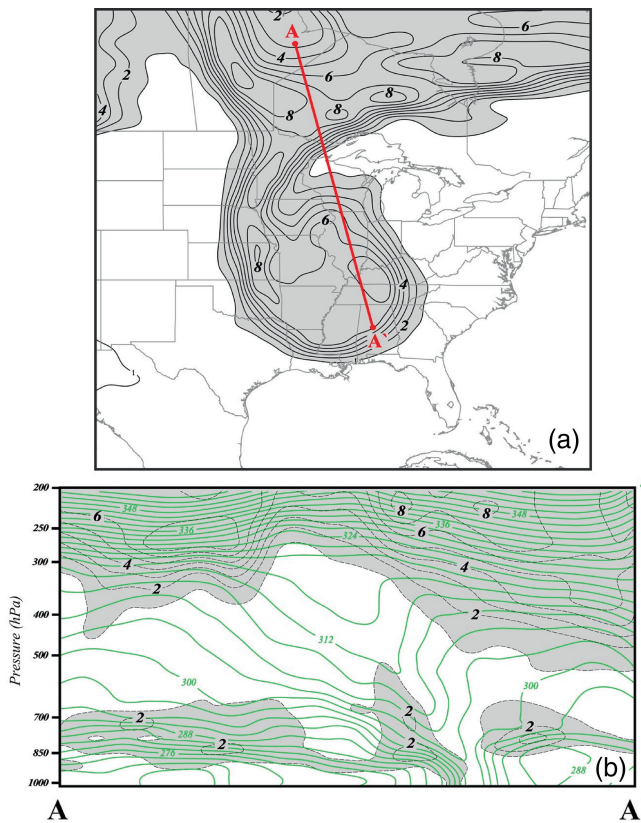


FIGURE 3 Illustration of the relationship between the treble clef tropopause-level potential vorticity (PV) distribution and the occluded thermal structure in the underlying troposphere. (a) Tropopause-level (250:300 hPa) PV from the CFSR analysis valid at 1800 UTC 19 January 1995. PV is labeled in potential vorticity units (PVU) ($1 \text{ PVU} = 10^{-6} \text{ m}^2 \text{ s}^{-1} \text{ K kg}^{-1}$) and shaded every 1 PVU starting at 1 PVU. Cross-section along line A–A' is shown in Figure 3b. (b) Cross-section along A–A' in Figure 3a of θ_e (thin green lines) labeled in K and contoured every 3 K. Gray shading is PV labeled in PVU and shaded every 1 PVU beginning at 1 PVU

Raymond, 1992), provided a convenient framework for Posselt and Martin (2004) to investigate the influence of LHR on the formation of an occluded thermal structure.

Comparing full physics and “no LHR” MM5 simulations of a major winter storm, Posselt and Martin (2004) found that the former depicted the canonical, troposphere-deep, warm-occluded structure while the latter produced only a shallow, poorly developed one. Their analysis showed that direct dilution of a local, upper-tropospheric PV maximum by mid-tropospheric LHR initiated formation of a local, upper-tropospheric PV minimum, or low-PV tongue, to the northwest of the surface cyclone center. The production of this PV minimum initiated a cutting off of the upper-tropospheric PV anomaly associated with the surface development. The associated upper-tropospheric circulation then forced the advection of low ($<1 \text{ PVU}$ [potential vorticity units])

values of PV into the developing PV trough. This combination of kinematic and diabatic processes acted to produce both the tropopause PV treble clef as well as the underlying warm-occluded thermal structure in the full physics simulation. In contrast, though an adiabatic kinematic tendency for production of a treble-clef PV morphology also operated in the “no LHR” simulation, the resulting PV and thermal structures were weaker and slower to evolve than those produced in the full physics simulation. Thus, the authors suggested that LHR plays an important role in the production of the characteristic occluded thermal structures observed in nature.

A number of methods have been proposed for objective identification of cold and warm fronts (e.g., Hewson, 1998; Hewson and Tittley, 2010; Berry *et al.*, 2011; Simmonds *et al.*, 2012; Schemm *et al.*, 2018; Thomas and Schultz, 2019a, 2019b and references therein). Naud *et al.* (2012, 2015, 2018), (Schultz, 2018) employed satellite-based radar and lidar profiles (CloudSat, Stephens *et al.*, 2002; CALIPSO, Winker *et al.*, 2009) to explore the cloud and precipitation distributions associated with objectively identified cold and warm fronts and how these distributions relate to the larger-scale environment. Although occlusions are a well-studied meteorological phenomenon (e.g., Schultz and Mass, 1993; Martin, 1998a, 1998b, 1999a, 1999b; Stoelinga *et al.*, 2002; Posselt and Martin, 2004; Schultz and Vaughan, 2011), there is no automated method of occlusion detection. Consequently, it has not been possible to consider the global distribution of occluded cyclones, their composite thermodynamic and kinematic structures or explore the cloud and precipitation distributions of a very large number of occluded sectors observed in a wide range of locations and environmental conditions.

Extratropical (ETCs) cyclones are responsible for the largest share of the global redistribution of heat required to offset latitudinal differences in radiative transfer. Since the occluded sectors of these storms are known to be regions of significant moisture convergence and attendant LHR, occluded cyclones provide a key physical link in the global energy and water cycles. As we peer into the future with sophisticated global climate models, it is essential that these models faithfully reproduce increasingly detailed aspects of the life cycles of the individual weather systems involved in these global cycles. This paper will lay the foundation for assessment of the climatological characteristics of occluded mid-latitude cyclones and attendant evaluation of the skill with which a global climate model can reproduce the canonical occluded structure and precipitation characteristics.

Central to the present study will be the description of an automated scheme that identifies the occluded sectors of cyclones from gridded reanalyses and/or climate model

output. The method will then be employed to construct the first global survey of occluded cyclones. In Section 2, we describe details of the objective identification scheme. Some results of its application to 11 years of MERRA-2 reanalysis data are presented in Section 3. Included in this presentation are a limited global climatology as well as composites of the thermal structure and vertical-motion distributions of wintertime occluded cyclones observed in both the Northern (NH) and Southern Hemispheres (SH) over 11 recent winters. A discussion of the results and an outline of future work to be undertaken using the identification scheme are offered in Section 4.

2 | AUTOMATION OF OCCLUSION IDENTIFICATION: METHODOLOGY

2.1 | Data

In the automated methodology to be described, the analysis uses 11 years of data from the second iteration of NASA's Modern-Era Retrospective analysis for Research and Application (MERRA-2) gridded reanalysis output (Gelaro *et al.*, 2017) spanning September 2006–August 2017. In particular, air temperature along with SLP, geopotential height, specific humidity and vertical velocity are utilized to identify occluded extratropical cyclones and subsequently portray aspects of their structure and evolution. The MERRA-2 data are available on a $0.625^\circ \times 0.5^\circ$ horizontal grid with 42 vertical levels spanning from 1,000 hPa to 3 hPa. For purposes of evaluation of the automated identification method to be described later, and to ensure it is reliable across different datasets and grid resolutions, the study also employed the NCEP Climate Forecast System Reanalysis (CFSR) (Saha, 2010) dataset, from which the same variables were available at 64 vertical levels with 38-km spatial resolution.

2.2 | Objective identification parameter

Since occlusion represents the beginning of the post-mature phase of a cyclone's life cycle, many (though not all) storms that occlude do so near their peak intensities. This study considers the time of peak intensity as the time at which either the central SLP reaches a minimum or when the pressure depth has reached a maximum, then choosing whichever phenomenon occurs first. Pressure depth is defined as the difference between the outermost closed SLP contour and the central pressure in Polly and Rossow (2016).

An occluded thermal ridge serves as a two-dimensional (2) proxy for the 3D TROWAL, the essential structural

feature of the occluded sector. Therefore, it can be identified using any of several thermodynamic variables, including potential temperature (θ), equivalent potential temperature (θ_e) and 1,000:500 hPa thickness. Since the occluded thermal ridge routinely extends through a substantial depth of the troposphere, 1,000:500 hPa thickness, denoted as Φ' , was chosen as the focal variable for the objective identification scheme as it best captures the full 3D structure of the feature. Elements of the analysis method were found to be occasionally noisy at the high native resolution of the MERRA-2 data. This fact, coupled with a desire to construct an automated detection method that could eventually be applied to lower resolution output from global climate models, compelled coarsening the native resolution of the MERRA-2 data by a factor of 2. Hence, the thickness fields were processed on a $1.25^\circ \times 1^\circ$ horizontal grid. Objective identification of the occluded thickness ridge (OTR) is based upon examination of the functional form of the divergence of the unit vector in the direction of $\nabla\Phi'$, given by,

$$\hat{n} = \frac{\nabla\Phi'}{|\nabla\Phi'|}, \quad (1)$$

An example field of Φ' and \hat{n} for an occluded cyclone over the British Isles at 0600 UTC 7 January 2008 is shown in Figure 4a. The divergence of Equation (1), $\nabla \cdot \hat{n}$, takes the form,

$$\nabla \cdot \hat{n} = \nabla \cdot \frac{\nabla\Phi'}{|\nabla\Phi'|} = \frac{\nabla^2\Phi' |\nabla\Phi'| - \nabla\Phi' \cdot \nabla |\nabla\Phi'|}{|\nabla\Phi'|^2}, \quad (2)$$

using the quotient rule. The sign of the resulting expression is negative in the presence of a thickness ridge but, as shown in Figure 4b, it is also negative in many other locations unrelated to the OTR. In order to highlight those areas of $\nabla \cdot \hat{n}$ that are also associated with the largest thermal contrasts, the final form of the finding function (referred to as F) is weighted by the magnitude of the thickness gradient.

$$F = (\nabla \cdot \hat{n}) |\nabla\Phi'| = \nabla^2\Phi' - \hat{n} \cdot \nabla |\nabla\Phi'|. \quad (3)$$

From this expression it is clear that F highlights regions where the Laplacian (i.e., divergence of the gradient) of the thickness field is substantial and/or where there is substantial advection of thickness gradient magnitude by the unit vector. In the vicinity of a thickness ridge, bounded by thickness contrasts on its flanking sides, both of these terms contribute to $F < 0$. Unfiltered fields of F contain small-scale features that can cloud the intended thickness ridge identification results. To avoid such obfuscation, only values of $F < -1 \times 10^{-9} \text{ m}^{-1}$ (F_{\max}) are considered and a five-point smoother is applied to avoid excessive noise in

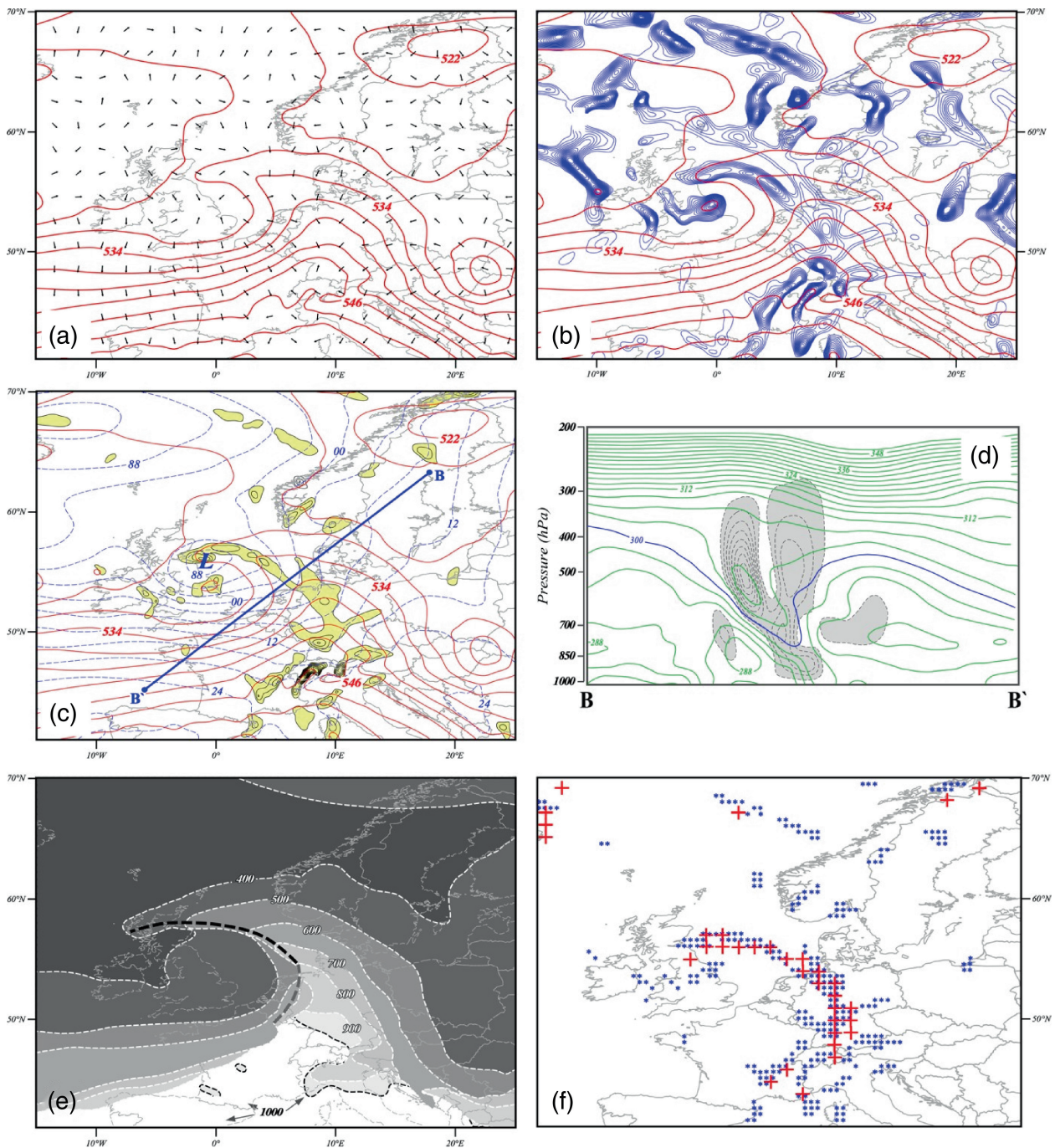


FIGURE 4 (a) 1000:500 hPa thickness (solid red) and \hat{n} , the unit vector in the direction of $\nabla\phi'$, from the Climate Forecast System Reanalysis (CFSR) valid at 0600 UTC 7 January 2008. Thickness is labeled in dam and contoured every 6 dam. Unit vectors are portrayed at every fifth grid point for clarity of presentation. (b) 1000:500 hPa thickness (solid red) labeled and contoured as in Figure 4a. Convergence of \hat{n} (thin blue lines) contoured every $-1 \times 10^{-5} \text{ m}^{-1}$ starting at $-1 \times 10^{-5} \text{ m}^{-1}$. (c) Sea-level isobars (dashed blue) and 1000:500 hPa thickness (solid red) from the CFSR valid at 0600 UTC 7 January 2008. Isobars labeled in hPa (with leading “9” or “10” missing) and contoured every 4 hPa. Thickness labeled and contoured as in Figure 4a. Negative F parameter (see text) shaded in yellow and contoured every $-1 \times 10^{-9} \text{ m}^{-1}$ starting at $-1 \times 10^{-9} \text{ m}^{-1}$. Vertical cross-section along B–B' is shown in Figure 4d. (d) Vertical cross-section of θ_e and ω along line B–B' in Figure 4c. θ_e labeled in K and contoured every 3 K with the 300 K isoline colored in blue. Upward vertical motion (gray shading) labeled in dPa s^{-1} and contoured every -2 dPa s^{-1} starting at -2 dPa s^{-1} . (e) Isobaric topography of the 300-K θ_e surface from the same CFSR dataset. Thin dashed white lines are isobars on that surface and the thick dashed line is the location of the TROWAL (TROugh of Warm air ALoft). (f) Blue asterisks identify CFSR grid points at which $F < -1 \times 10^{-9} \text{ m}^{-1}$ at 0600 UTC 7 January 2008. Red crosses identify points on the coarsened MERRA-2 grid at which $F < -1 \times 10^{-9} \text{ m}^{-1}$ at the same time. These grid points are highlighted as black crosses surrounded by gray squares in Figure 5e

the output. The example shown in Figure 4c is illustrative of the efficacy of F as the noisiness of the raw $\nabla \cdot \hat{n}$ field in Figure 4b is rendered considerably more coherent and interpretable. The main feature is an extended region of $F < F_{\max}$, some of which clearly coincides with the axis of the 1,000:500-hPa thickness ridge, while the other portion stretching from southern Germany across eastern France appears just ahead of the cold-frontal thickness gradient. The vertical cross-section along B–B' in Figure 4c cuts through that section of the F field that elongates along the thickness ridge from the low-pressure center into the warm sector.

That cross-section (Figure 4d) illustrates the canonical warm-occluded thermal structure with an axis of maximum θ_e between two baroclinic zones, the warm and cold fronts, sloping poleward with height. Martin (2006) characterizes the location at which the axis of maximum θ_e intersects with the ground as the position of the surface warm occluded front. As is generally the case, a plume of maximum vertical motion associated with the main updraft of the storm appears to be better collocated with the TROWAL than with the surface-occluded front. The isobaric topography of the 300-K moist isentrope from this case is shown in Figure 4e. This particular isentrope was chosen as it lies near the warm edge of both the cold and warm fronts in the occluded thermal structure. The TROWAL, indicated by the bold dashed line, clearly coincides with the northern portion of the $F < F_{\max}$ region. However, by its nature as the 3D sloping intersection of the cold and warm fronts of the occluded thermal structure, the TROWAL is never perfectly represented by analysis at a single level or in a single layer. Despite the fact that there is no objective standard against which the automated identification method could be checked, elements of the canonical occluded thermal structure are easy to identify in gridded reanalysis datasets, as demonstrated in the example illustrated in Figure 4. Therefore, our evaluation of F consisted of interrogating every feature the parameter flagged as occluded in the north Atlantic and north Pacific basins during winters 2007–2008 and 2008–2009 against those canonical elements. An example of a direct comparison of the depiction of an occlusion identification by both the MERRA-2 and CFSR datasets (of which many were considered) is shown in Figure 4f. As will be described in the next section, use of F with some synoptically informed qualifications has proven to be satisfactory as the composite results will unambiguously testify. Because we did not set out to develop a method to assist operational forecasters, the assessment of F was work product and not formally recorded. In order to develop a robust, dataset-independent technique, an element of that testing was employment of a collection of input datasets including

NCEP-CFSR as well as NCEP-NCAR reanalysis data (Kalnay *et al.*, 1996).

2.3 | The cluster-tracking method

Automating the use of the F parameter presents the unique opportunity to identify all extratropical cyclones undergoing occlusion as well as construct composites of elements of the thermodynamic and kinematic structure of the occluded sector. Given its versatility, F can be employed using output from any gridded dataset, such as those produced by standard numerical weather prediction (NWP) forecast models and/or global climate models (GCMs). This study employs the same cyclone database as used in Naud *et al.* (2012, 2015), which tracked and identified storms using the NASA Modeling, Analysis, and Prediction (MAP) Climatology of Mid-Latitude Storm area (MCMS) algorithm developed by Bauer and Del Genio (2006) and Bauer *et al.* (2016) applied to the ERA-Interim six-hour (hereafter, 6-hr) SLP fields (Dee *et al.*, 2011). The MCMS algorithm searches for local minima in SLP and tracks them through time. Qualifying cyclones must not travel more than 720 km in any 6-hr interval of their life cycles but must travel at least 700 km, exist for at least 24 hr, and reach a minimum SLP of less than 1,010 hPa during their life cycles.

The full track of each identified storm in the cyclone database was considered and divided into individual snapshots, depicting the instantaneous state of the cyclone every 6 hr. Automating the use of the OTR finding function, F , to identify cyclones that are occluded involves several assessments at each 6-hr snapshot for candidate cyclones. First, the individual cyclone tracks have to be identified. Figure 5a provides an example of the track of a sample cyclone that occurred over the northeast Atlantic in early January 2008 (the analysis in Figure 4 represents one 6-hr snapshot of this storm). The cyclone's time of peak intensity is clearly indicated as is its position every 6 hr from 0600 UTC 6 January 2008 to 1800 UTC 8 January 2008. To ensure computational efficiency, a limited area stretching from -10° to $+20^\circ$ longitude and $\pm 20^\circ$ latitude from the storm center, is then considered at each 6-hr analysis time. MERRA-2 temperature, SLP, 1000:500 hPa thickness, θ_e and vertical velocity fields were collected within this limited area and F was calculated at each grid point.

The finding function is then applied within this area, flagging grid points at which $F < F_{\max}$. Corresponding points for the example time previously considered (Figure 4) are shown as the red crosses in Figure 4f. The collection of such points, in the prescribed limited area, for 1200 UTC 6 January 2008 are indicated by the black

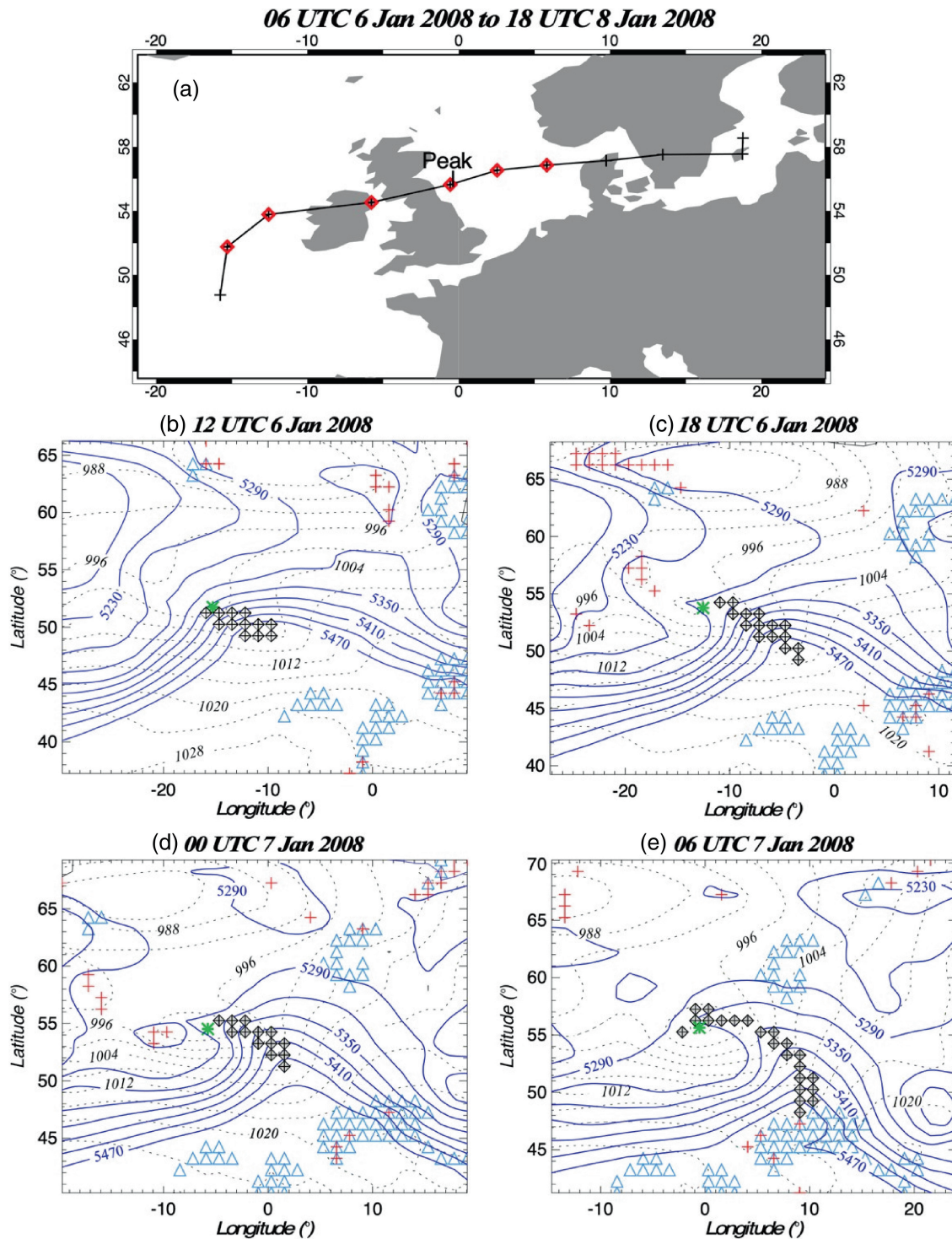
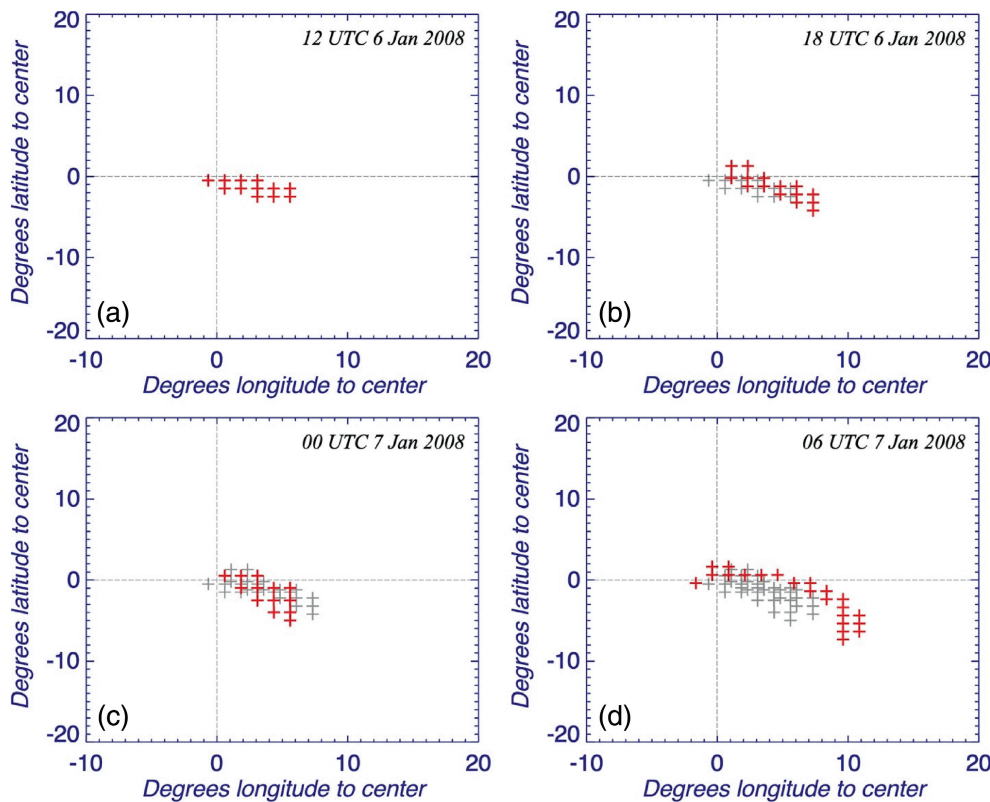


FIGURE 5 Illustration of the cluster tracking method. (a) Track of a cyclone in the north Atlantic from 0600 UTC 6 January to 1800 UTC 8 January 2008 from the MERRA-2 reanalysis data. Crosses represent the position of the cyclone center at each 6-hr time, red squares indicate times at which a qualifying cluster deemed the storm occluded, and “Peak” indicates the time and location of the storm’s peak intensity. (b) 1000:500 hPa thickness (blue solid lines) and sea-level isobars (SLP, dotted black lines) at 1200 UTC 6 January 2008 from the MERRA-2 reanalysis data. Thickness is labeled in m and contoured every 60 m. SLP is labeled in hPa and contoured every 4 hPa. Red and black crosses are gridpoints at which $F < F_{max}$. Blue triangles are gridpoints at which $STDSurf_{max}$ exceeds 300 m. Green star is the location of the SLP minimum. Black crosses with gray shaded squares represent grid points in a qualifying cluster (see text for explanation). (c) As for Figure 5b but for 1800 UTC 6 January 2008. (d) As for Figure 5b but for 0000 UTC 7 January 2008. (e) As for Figure 5b but for 0600 UTC 7 January 2008, time of peak intensity


FIGURE 6

Cyclone-relative grid with SLP minimum at (0,0). (a) Red crosses indicate the qualifying cluster identified at 1200 UTC 6 January 2008 for the cyclone whose track is considered in Figure 5. (b) As for Figure 6a but with red crosses indicating the qualifying cluster identified at 1800 UTC 6 January 2008 and the gray crosses indicating qualifying clusters identified at all prior 6-hr snapshots of the cyclone depicted in Figure 5. (c) As for Figure 6a but with red crosses indicating the qualifying cluster identified at 0000 UTC 7 January 2008. (d) As for Figure 6a but with red crosses indicating the qualifying cluster at 0600 UTC 7 January 2008

and red crosses in Figure 5b (and similarly for other times in Figures 5c–e). These points are referred to as qualifying grid points. Any such grid points are given no further consideration if the standard deviation of the surface elevation amongst the group formed by the object grid point and its four neighbors is greater than 300 m, $STDSurf_{max}$. Such points in the example storm are indicated with a blue triangle in Figures 5b–e. Remaining grid points meeting the threshold in F qualify for further consideration *only when* at least 8 (N_{min}) contiguous neighbors constitute a cluster *and* the mean longitude of that cluster is located to the east of the SLP minimum (note 12 such grid points in Figure 5b). Such qualifying clusters have a black diamond surrounding a black cross in Figures 5b–e. When a 6-hr snapshot possesses a qualifying cluster it is said to be an *occlusion identification*. In order to have identified an *occluded ETC*, qualifying clusters must at least partially overlap in a cyclone-relative grid at at least two consecutive 6-hr times as illustrated in Figure 6 for the 6–7 January 2008 cyclone. This confirms that the cyclone center and the qualifying cluster are moving in tandem. Additionally, the first appearance of a qualifying cluster in a cyclone’s track history (e.g., the cluster at 1200 UTC 6 January 2008 in Figure 5b) must have been located within a distance of 300 km (D_{max}) of the cyclone center in order for the cyclone to qualify as an occluded ETC and be included in the subsequent composite analyses. Finally, if a cluster is identified (1) only once during a cyclone’s life cycle, (2) at

several non-consecutive 6-hr time steps, or (3) in a consecutive series that ends *before* the cyclone reaches its peak intensity, that storm and its cluster are not considered in any subsequent analyses. These various disqualifications reflect the intentionally conservative nature of the scheme which is designed to minimize false identification. Though such a design may overlook some weak occlusions, given the large number of candidate storms, the slightly conservative approach adopted here is unlikely to lead to mischaracterization of the global climatology or composite structures.

This procedure can be applied to any gridded datasets with only slight modifications made based upon horizontal grid spacing. Resolution-based adjustment made to several of the parameters involved in the method are summarized in Table 1. The parameters F_{max} , N_{min} , and $STDSurf_{max}$ were determined to exhibit a linear dependence on grid resolution. D_{max} is an absolute distance and, therefore, its magnitude remains the same for all three grid spacings.

Employing each 6-hr occlusion identification, the following procedure was employed to build composite vertical cross-sections through these features. The procedure is best described using a schematic version (Figure 7) of a single 6-hr identification period (such as those shown in Figures 5b–e). The procedure takes advantage of the fact that the occluded thermal ridge can be accurately portrayed by a number of alternatives to 1,000:500 hPa

TABLE 1 Parameter values for each dataset and grid resolution used in this study

	MERRA-2 (1.25° × 1°)	MERRA-2 (2.5° × 2°)	NCEP-NCAR (2.5° × 2.5°)
F_{\max}	-10^{-9} m^{-1}	$-0.5 \times 10^{-9} \text{ m}^{-1}$	$-0.5 \times 10^{-9} \text{ m}^{-1}$
N_{\min}	8	4	4
STDSurf _{max}	300 m	150 m	150 m
D_{\max}	300 km	300 km	300 km

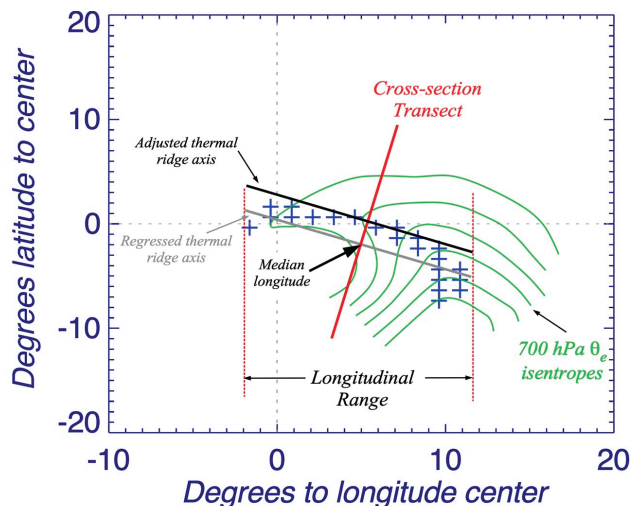


FIGURE 7 Illustration of the method by which the composite cross-section transect line is determined for the automated occlusion identification. Blue crosses are schematic grid points constituting a qualifying cluster. Green solid lines are 700-hPa θ_e isentropes. Red solid line is the cross-section transect line

thickness, including 700-hPa θ_e . It proceeds by first calculating a regression line (in latitude and longitude) through the cluster of the grid points constituting a qualifying cluster (blue crosses in Figure 7). That line, the solid gray line in Figure 7, represents the thickness ridge axis and its longitudinal range is bounded by the dashed red lines. At the median longitude of the thickness ridge axis, a transect is drawn perpendicular to the axis. Finally, the thickness ridge axis line is slid along the transect line until it reaches the coincident 700-hPa θ_e maximum. Synoptic experience suggests that the OTR rarely extends above 350 hPa. Consequently, though a number of other choices might also serve the purpose, 700 hPa represents a mid-tropospheric level (free from excessive boundary-layer influences) by which to normalize the position of the axis of the thickness ridge. The intersection of the transect line and the adjusted thermal ridge axis is then the midpoint of a 3,000-km-long transect line along which any variable (θ_e , ω , T , etc.) may be obtained. In order to produce composites of the vertical structure through the OTR, each such transect is preserved and then they are all averaged together to produce the composite vertical cross-section of the given variable.

Because the middle of each transect is, by construction, coincident with the maximum 700-hPa θ_e for that particular cross-section, it is possible to create separate composite occluded structures based upon ranges of their maximum 700-hPa θ_e values.

3 | SOME CLIMATOLOGICAL APPLICATIONS

Because subsequent work will employ observations made with CloudSat/CALIPSO data, application of the automated method just described has been applied to 11 years (1 September 2006–31 August 2017) of MERRA-2 reanalyses, corresponding to the CloudSat/CALIPSO era. In that period 6,147 individual cyclone tracks (2,529 in the NH and 3,618 in the SH) have been identified from which 26,351 6-hrly snapshots (as described in Section 2c) have resulted in occlusion identifications. Given the standard deviation of surface elevation criteria previously described (STDSurf_{max}), the analysis focused only on those identifications that were made over the oceans. Thus, a total of 22,329 identifications (8,741 in the NH and 13,588 in the SH) were included in the analysis. In the next section descriptions of some elements of these occlusion identifications are presented.

3.1 | Global distribution of occluded cyclones

Employing the automated identification method just described, a global distribution of occluded identifications can be constructed. Figure 8a shows the NH winter (DJF) cumulative distribution of 6-hr occluded identifications over the 11-year period and reveals that, in the north Pacific, occluded cyclones populate the basin poleward of the mean jet with distinct maxima in the southern Sea of Okhotsk, east of the Kamchatka peninsula, and in the Gulf of Alaska. Wintertime occlusions in the north Atlantic basin are concentrated in a strip running from the mouth of the Labrador Sea to the southeast coast of

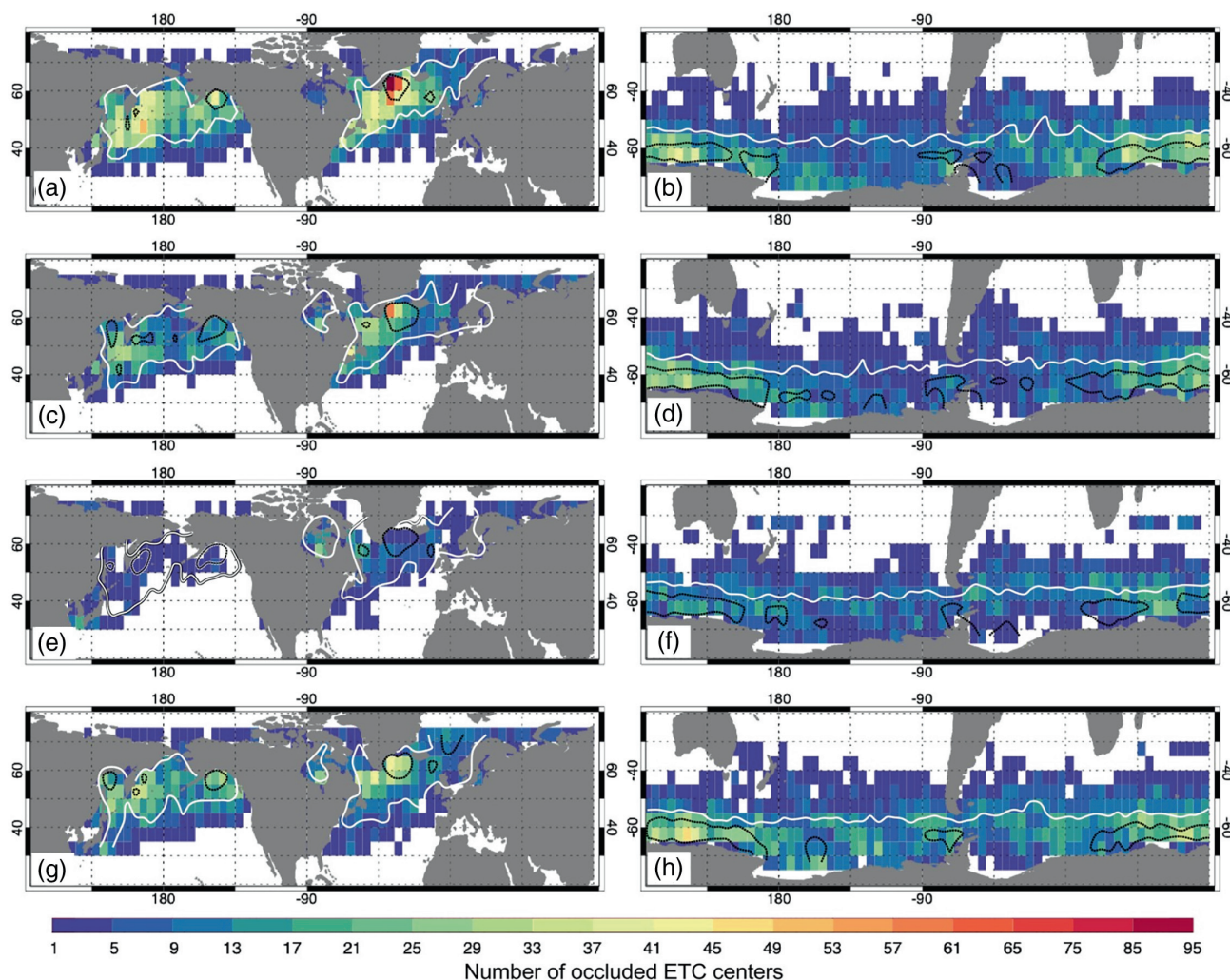


FIGURE 8 Distribution of all (6-hr) Extratropical cyclone (ETC) centers that are occluded organized by hemisphere and season. Color bar refers to the number of occluded identifications per $5^{\circ} \times 5^{\circ}$ box in (a) Northern-Hemisphere (NH) winter (DJF), (b) Southern-Hemisphere (SH) winter (JJA), (c) NH spring (MAM), (d) SH spring (SON), (e) NH summer (JJA), (f) SH summer (DJF), (g) NH autumn (SON), and (h) SH autumn (MAM). Solid white (dashed black) lines in each panel indicate the 100 (150) cyclones per grid box contour for the given season

Greenland. Further analysis (not shown) revealed that the robust maximum in occluded identifications near the tip of Greenland in Figure 8a is a function of a larger overall number of storms there and *not* an unusually large proportion of those storms occluding in that location. The two winter maxima regions harbor smaller numbers of occlusion identifications during the NH spring (MAM) (Figure 8c). Identifications are considerably less common during the NH summer (JJA) while frequenting the same general locations (Figure 8e). The number of occluded identifications quickly rebounds in NH autumn (SON) (Figure 8g).

The distribution in the SH is different in many respects. The wintertime (JJA) distribution shows almost no occlusion identifications equatorward of 40° S (Figure 8b). Despite the fact that a noted cyclogenesis maximum exists in the lee of the Andes during austral winter (Hoskins

and Hodges, 2005), there is no coincident maximum in occluded identifications in the region in that season. Instead, cyclones in the lee of the Andes appear to occlude more frequently in spring (Figure 8d) and autumn (Figure 8f). Dual frequency maxima during winter appear along the Wilkes Land (120° E) and Enderby Land (45° E) coasts of Antarctica. By spring (SON), occluded identifications are less common everywhere with the greatest decreases observed in the longitudes straddling South America (Figure 8d). The distribution thins further by austral summer (DJF) (Figure 8f). With a resurgence of occluded identifications at the locations of the winter maxima and a general increase elsewhere, autumn (MAM) is the season with the greatest number of identifications in the SH (Figure 8h). Thus, the hemispheres have notably different seasonal cycles in occluded identifications.

3.2 | Structure of composite Northern-Hemisphere wintertime occlusions

Further detail regarding the wintertime distribution of NH occlusion identifications is afforded by stratifying them by the value of the 700-hPa θ_e maximum along the thickness ridge axis. The goal was to partition the total number of identifications into as many groups as possible whose composite structures were meaningfully different from one another while keeping the number of identifications in each group large enough to ensure statistical robustness. Such a compromise was achieved by considering six groups each containing 372 occluded ETCs. Figure 9 shows the number of occluded identifications in six bins constructed such that each bin contains the same fraction of the total number of identifications in the 2006–2017 analysis period. Two-thirds of all the identifications had 700-hPa θ_e maxima in the range of approximately 293 K to 313 K. The geographic distribution from each of these six bins is shown in Figure 10. Not surprisingly, stratification by 700-hPa θ_e maxima effectively separates subpopulations of identifications by latitude, with the lowest θ_e maxima occurring at high latitudes and vice versa. Bins II–IV (Figures 10b–d) exhibit distributions of occluded identifications that are broadly consistent with the climatological positions of the Aleutian Low in the Pacific basin and the Icelandic Low in the Atlantic basin. In the two “warmest” bins (Figures 10e,f), however, the occluded identifications in both basins notably recede equatorward from these centers.

Figure 11 presents the results of constructing composite vertical cross-sections of θ_e through each of these six

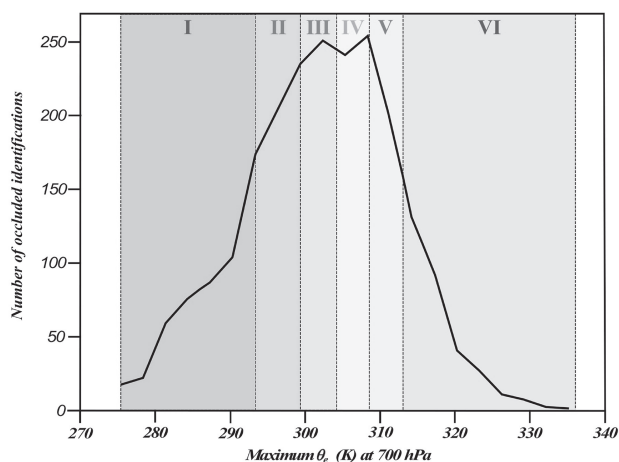


FIGURE 9 Cumulative distribution function of all Northern-Hemisphere (NH) wintertime occluded identifications stratified by the 700 hPa θ_e maximum along their respective thermal ridge axes. The six groups are referred to as Bins I–VI in the text [Colour figure can be viewed at wileyonlinelibrary.com]

groups of occlusion identifications. Recall from Figure 9 that the 700-hPa θ_e maxima of those comprising Bin I range from 275 K to 293 K. In this “coldest” bin, the OTR notably does not exhibit any vertical tilt (Figure 11a), suggesting that these storms have a shallower and less developed occluded thermal structure than those occurring at lower latitudes. These identifications are associated with cyclones that appear to cluster near coastlines – especially around Kamchatka and southeast Greenland (Figure 11a). This circumstance may influence their composite structure compared to those cyclones found farther out at sea. Both the cold- and warm-frontal portions of the composite occluded structure in Bin II (Figure 11b) are better developed than those in Figure 11a. The successively “warmer” composite occlusions (Figure 11c–f) exhibit increasingly robust cold- and warm-frontal structures as well as axes of maximum θ_e that tilt increasingly poleward, as in the canonical occluded thermal structure. Also notable in these last four composites is the burgeoning couplet of lower-tropospheric cyclonic PV (at the center of the cross-sections) along with its companion upper-tropospheric PV minimum. These features are physically linked to each other through the substantial mid-tropospheric LHR that characterizes the TROWAL in these “warmer” storms.

Further evidence of this connection is evident in the composite vertical motions in the vicinity of the OTRs of these different collections of occlusion identifications shown in Figure 12. It is immediately apparent that the “warmer” identifications have stronger upward vertical motions within their OTRs and that their composite vertical motion plumes share the poleward tilt of their respective axes of maximum θ_e . The magnitude of ω is a function of the forcing for ascent modulated by the local static stability. As noted in reference to Figure 10, stratifying the identifications by 700-hPa θ_e maxima in their OTRs amounts to a sorting by latitude. Thus, the “warmer” (i.e., lower-latitude) ones are consistently farther south over warmer sea-surface temperatures and are therefore likely characterized by weaker stratification in their warm sectors prior to occlusion. Martin (1999a) showed that synoptic-scale forcing during the process of occlusion (namely, positive vorticity advection [PVA] by the thermal wind [Sutcliffe, 1947]) thrusts some portion of this warm-sector air aloft into the TROWAL. Nearly all the occluded identifications shown in Figure 10 occur in proximity to the NH storm tracks (see Figure 8a) which, by definition, are regions of maximum frequency of surface development. Since a fundamental synoptic-scale forcing for ascent in mid-latitude cyclogenetic environments is provided by PVA by the thermal wind (e.g., Sutcliffe, 1947; Trenberth, 1978; Hoskins *et al.*, 1978; Hoskins, 1999; Martin, 1999a, 1999b), it is reasonable to conclude that the vast

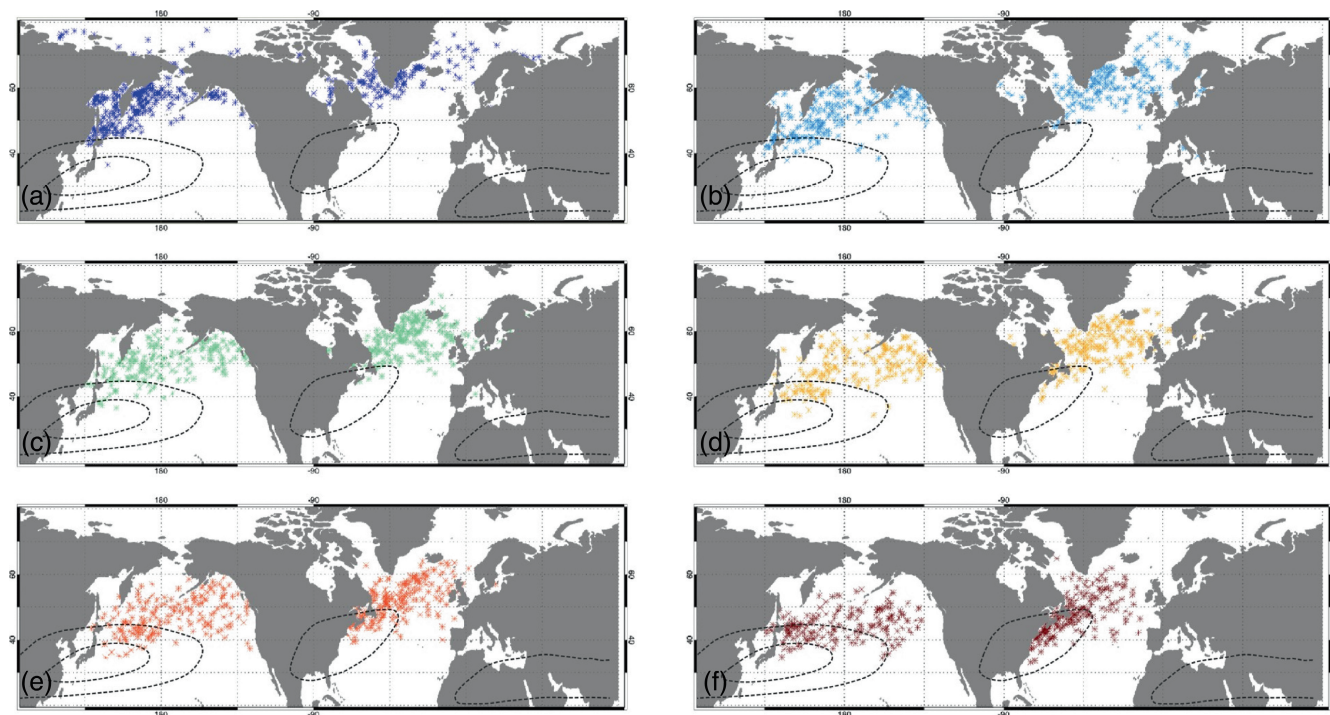


FIGURE 10 Geographic distribution of Extratropical cyclone (ETC) centers that are occluded in (a) Bin I, (b) Bin II, (c) Bin III, (d) Bin IV, (e), Bin V, and (f) Bin VI as identified in Figure 9. Dashed lines are the DJF average 30 and 50 m s^{-1} isotachs at 300 hPa from 2006 to 2017 from the MERRA-2 reanalysis

majority of occluded identifications shown in Figure 10 occurred in regions where PVA by the thermal wind was involved in development. We suggest that the robust differences in response to such forcing, as manifested in the notable differences in vertical motion, are at least partly, and perhaps largely, a function of the decreasingly stable stratification at lower latitudes.

3.3 | Structure of composite Southern-Hemisphere wintertime occlusions

As in the preceding subsection, the wintertime distribution of occlusion identifications is divided into six groups with equal populations of 605 occluded SH ETCs based upon the value of the 700-hPa θ_e maximum along the thickness ridge axis. Figure 13 shows the number of occluded identifications in each of those six groups. Two-thirds of all the identifications had 700-hPa θ_e maxima in the range of approximately 288 K to 304 K, notably lower than the θ_e range of the equivalent partition of NH occlusion identifications (Figure 9). It should also be noted that the number of wintertime occlusion identifications in the SH is nearly twice that of the NH during the same 11-year period (note the ordinate axis in Figure 13 vs Figure 9) and that the peak occurs at much lower θ_e

in the SH. The geographic distribution of occlusions from each of these six bins is shown in Figure 14. As in the NH, the stratification by 700-hPa θ_e maximum primarily separates subpopulations of identifications by latitude. An exception to this general rule is suggested by the notable maxima of occlusion identifications east of Argentina that appear in Bin VI (Figure 14f). This regional concentration of occluded ETCs suggests that the “warmest” events in the wintertime cyclogenesis maximum identified by Hoskins and Hodges (2005) are more likely to occlude than all others in that same region.

Figure 15 presents the composite vertical cross-sections of θ_e through each of the six groups of SH occlusion identifications. As in the NH population, the “coldest” composite does not exhibit any vertical tilt (Figure 15a). In fact, such a vertical tilt does not appear until the composites of Bin III (Figure 15c) and then becomes more exaggerated in the successively “warmer” bins (Figures 15d–f), as was the case for the NH composites. As in the “warmest” NH identifications, a relationship between expanding lower-tropospheric cyclonic (negative) PV features and a companion upper-tropospheric PV maxima is clearly evident in Figures 15c–f. Interestingly, even the “coldest” identifications are characterized by lower-tropospheric cyclonic PV maxima in the SH (Figures 15a,b). Another notable difference between the “warmest” SH composite occluded structures as compared

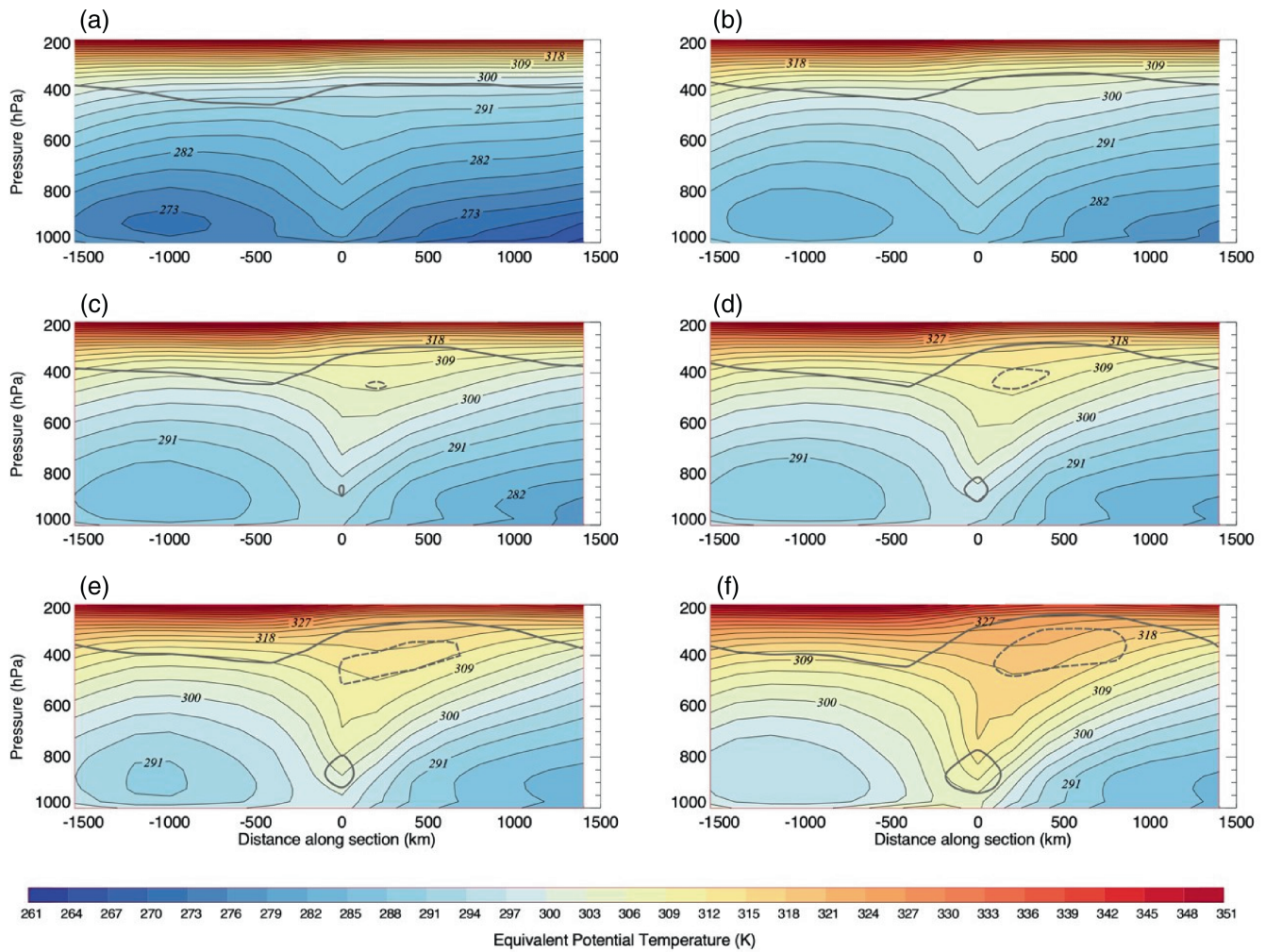


FIGURE 11 Composite vertical cross-sections of θ_e through the occluded thickness ridge (OTR) in occlusions comprising (a) Bin I, (b) Bin II, (c) Bin III, (d) Bin IV, (e) Bin V, and (f) Bin VI as identified in Figure 9. Black solid lines are θ_e isentropes labeled in K and contoured and shaded (according to legend) every 3 K. Thick solid (dashed) line is the 1.5 PVU (0.5 PVU) (potential vorticity units) isertel. Thin dotted line at $x = 0$ in each cross-section identifies the intersection of the composite transect line and the adjusted thermal ridge axis. Distance along the cross-section is indicated in km; positive to poleward and negative for equatorward

to their NH counterparts is that the axis of maximum θ_e does not penetrate to the surface in the SH composites (e.g., $\theta_e = 288$ K in Figure 15e and $\theta_e = 297$ K in Figure 15f). Instead, it appears that their occluded thermal structures are found atop a shallow, potentially unstable boundary layer in which θ_e decreases with height to approximately 950 hPa.

Finally, the composite vertical motions in the vicinity of the SH OTRs are shown in Figure 16. Again, as in the NH, the “warmer” occlusions are associated with stronger upward vertical motions within their OTRs as well as gradually increasing poleward tilt. The same conjunction of synoptic-scale forcing and stratification presumed to be involved in shaping the NH composites likely also determines the characteristics of the SH vertical motion composites. In the face of this probable similarity, it is interesting to note that both the horizontal and vertical

scales of the ascent in the SH composites are larger. Alternatively, the composite NH occluded-sector vertical motions are both more concentrated and more vigorous. Identification of the underlying physical factors that might account for this difference is the subject of ongoing research.

4 | DISCUSSION AND CONCLUSION

The post-mature phase of a mid-latitude cyclone is characterized by a 3D, sloping thermal ridge, that scientists at the Canadian Meteorological Service termed the TROWAL. The TROWAL is the essential structural feature of a warm-occluded cyclone, and its development not only links to cyclone dynamics, but also influences

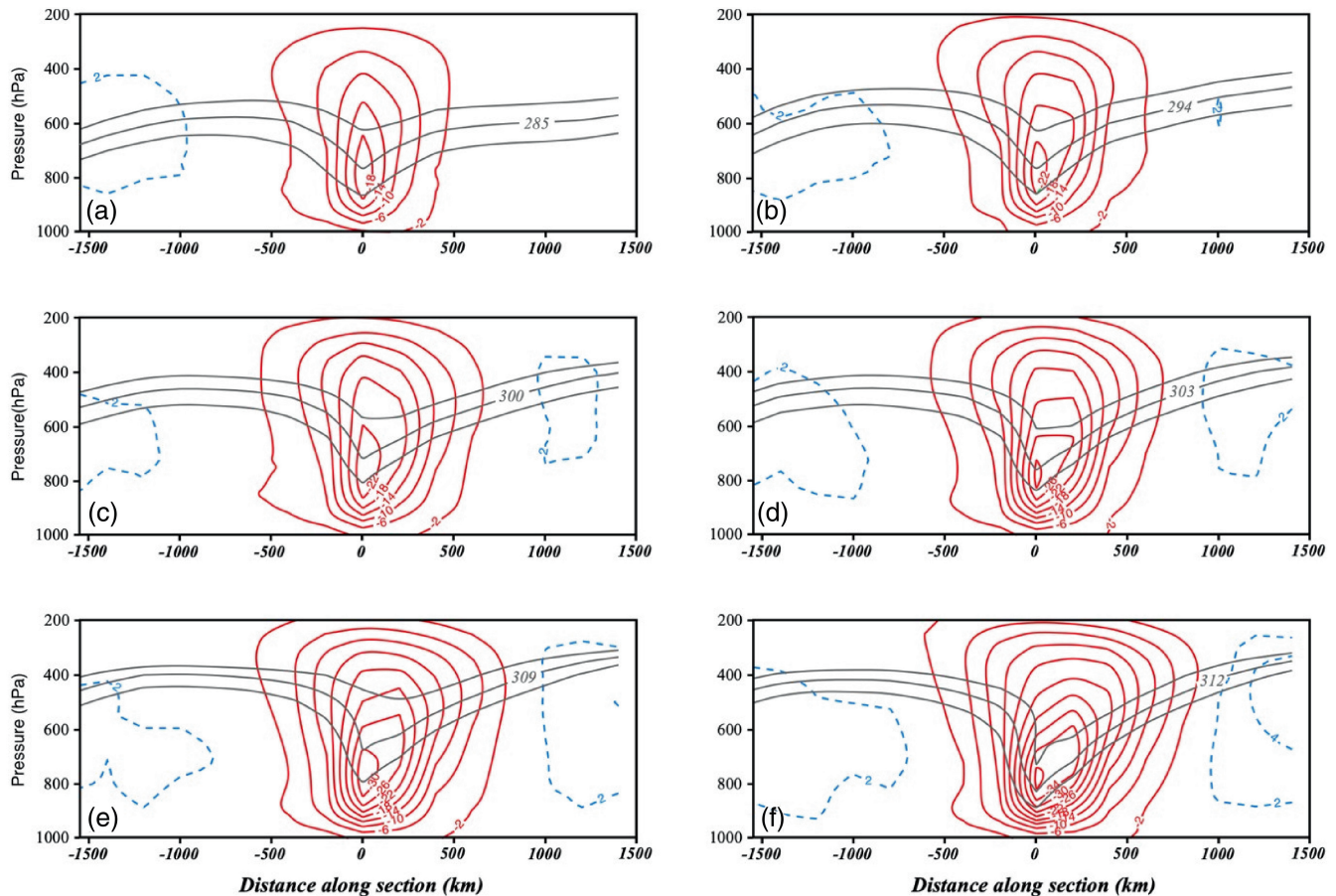


FIGURE 12 Composite vertical motions through the occluded thickness ridge (OTR) in occlusions comprising (a) Bin I, (b) Bin II, (c) Bin III, (d) Bin IV, (e) Bin V, and (f) Bin VI as identified in Figure 9. Thin solid red (dashed blue) lines are upward (downward) vertical motion labeled in units of dPa s^{-1} and contoured every 4 dPa s^{-1} starting at -2 (2) dPa s^{-1} . Thicker gray lines in each panel are three consecutive θ_e isentropes from the respective panels in Figure 11, each centered on the isentrope that straddles the 0 point along the x-axis at 700 hPa

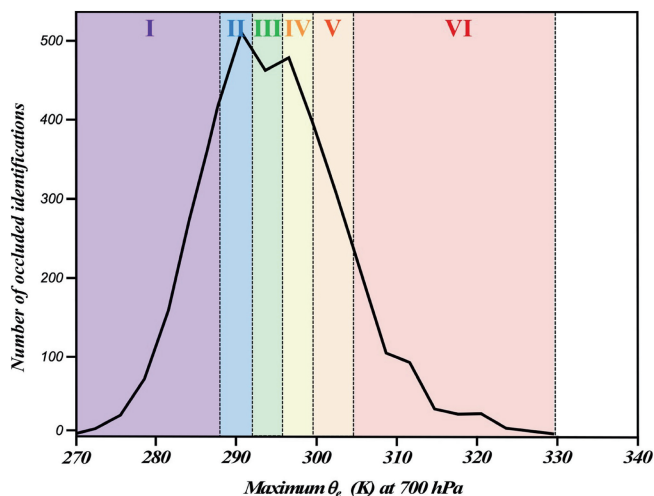


FIGURE 13 Cumulative distribution function of all Southern-Hemisphere (SH) wintertime occluded identifications stratified by the 700 hPa θ_e maximum along their respective thermal ridge axes. The six groups are referred to as Bins I–VI in the text

the distribution and intensity of precipitation. Though a number of studies (e.g., Wallace and Hobbs, 1977; Schultz and Mass, 1993; Martin, 1998a, 1998b, 1999a, 1999b; Posselt and Martin, 2004; Schultz and Vaughan, 2011) have considered the aspects of the structure, evolution and dynamics of occluded cyclones, there has been no attempt to develop an automated scheme to identify occlusions in gridded datasets. In fact, the present paper represents the first contribution that considers a climatology of occluded cyclones based upon identification of their canonical 3D thermal structure. Consequently, current understanding of the structural evolution, dynamics, and cloud and precipitation distribution associated with occluded cyclones is derived predominantly from the analyses of individual case studies and/or model simulations. In order to expand this rather limited perspective on investigations of the occluded stage of the cyclone life cycle, this study describes an automated method to identify such occluded thermal structures and illustrates its applications to the analysis of the global distribution of occluded cyclones, as well as

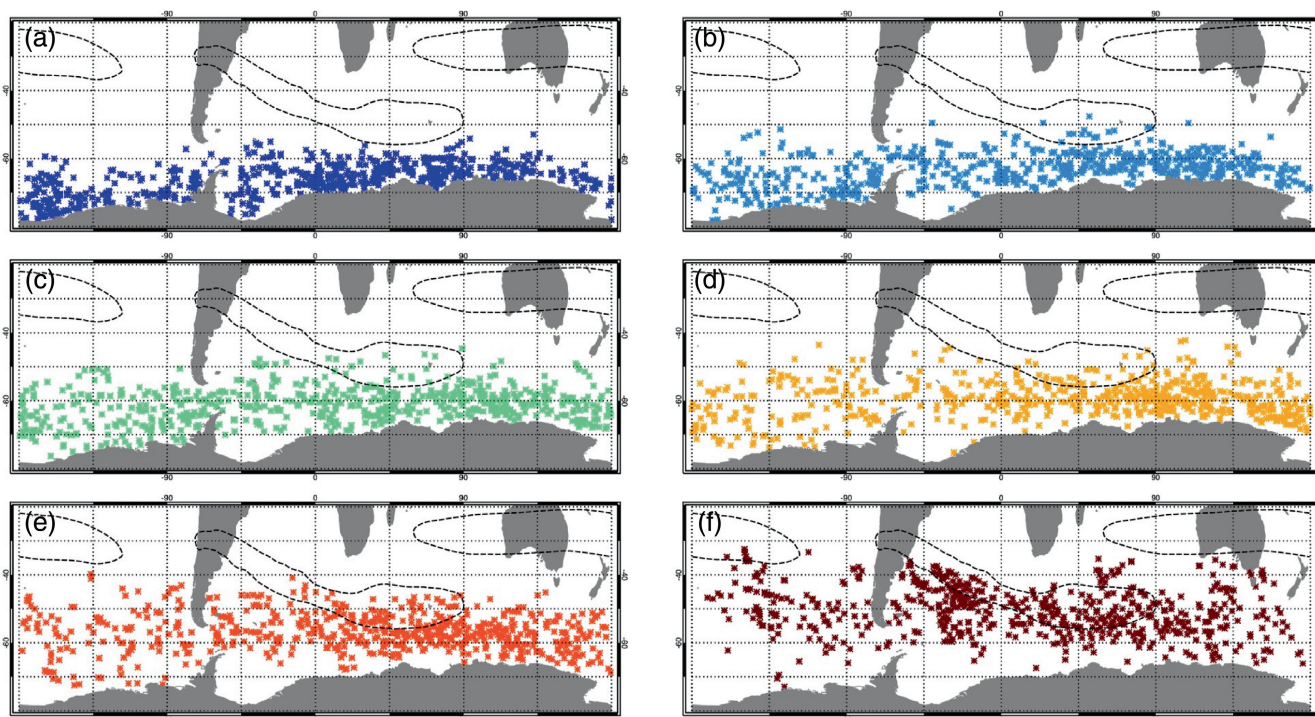


FIGURE 14 Geographic distribution of Southern-Hemisphere (SH) Extratropical cyclone (ETC) centers that are occluded in (a) Bin I, (b) Bin II, (c) Bin III, (d) Bin IV, (e), Bin V, and (f) Bin VI as identified in Figure 13. Dashed lines are the JJA average 30 m s^{-1} isotachs at 300 hPa from 2006 to 2017 from the MERRA-2 reanalysis

to the construction of composite cross-sections through the OTR.

The detection method, quantified using the F parameter defined in Equation (3), arises from evaluation of the divergence of the unit vector in the direction of the 1,000:500-hPa thickness gradient. Regions of convergence of the unit vector identify thickness ridges while regions of divergence detect thickness troughs. With only minor empirical adjustments, we find that the F parameter consistently and accurately identifies the OTR, and therefore, occluded cyclones, in any gridded dataset. Though it is possible to usefully employ the F parameter *without* a-priori knowledge of cyclone positions and tracks, our experience suggests that doing so invites a level of uncertainty that can compromise the results. Coupled with a cyclone-tracking algorithm, however, F can be used to identify the position and track of occluded cyclones around the globe. In this paper, we considered such distribution over the time period of 2006–2017 using the MERRA-2 dataset.

The analysis reveals that NH occlusions occur most frequently during the winter season (DJF) and most often poleward of the mean jet in the Pacific basin and in a strip from the Labrador Sea to the Greenland coast in the Atlantic Ocean. On the other hand, occlusions tend to occur poleward of 40° S throughout most of the year in the SH, and maximize in frequency in SH autumn

(MAM). Binning winter occluded identifications according to the value of their respective 700-hPa θ_e maximum along the thickness ridge axis allows for further categorization of these features, as well as new insights regarding the influence of the temperature and moisture of warm-sector air on the robustness of the resulting occluded thermal structures. Two-thirds of all NH occlusion identifications had a maximum 700-hPa θ_e in the range of 293–313 K, while the extremes ranged from as low as approximately 275 K to as high as approximately 335 K. In the SH, two-thirds of wintertime occlusion identifications had a lower maximum 700-hPa θ_e in the range of 288–304 K. Perhaps unsurprisingly, the analysis found that in both hemispheres the intensity of the composite vertical motion in the TROWAL was generally inversely proportional to the latitude at which the occlusion occurred, presumably as a result of less stably stratified air being found in the occluded sectors of warmer storms. The “colder” occlusion composites in both hemispheres also suggested that such high-latitude cyclones tend to have a shallower version of the canonical occluded thermal structure and also exhibit less tilt to the axis of maximum θ_e .

The variability in occluded thermal structures and in the intensity of the vertical motion characterizing the six groups of occlusions in each hemisphere are almost certainly physically related. Martin (1999a) found that that convergence of the along-isentrope (\vec{Q}_s) component

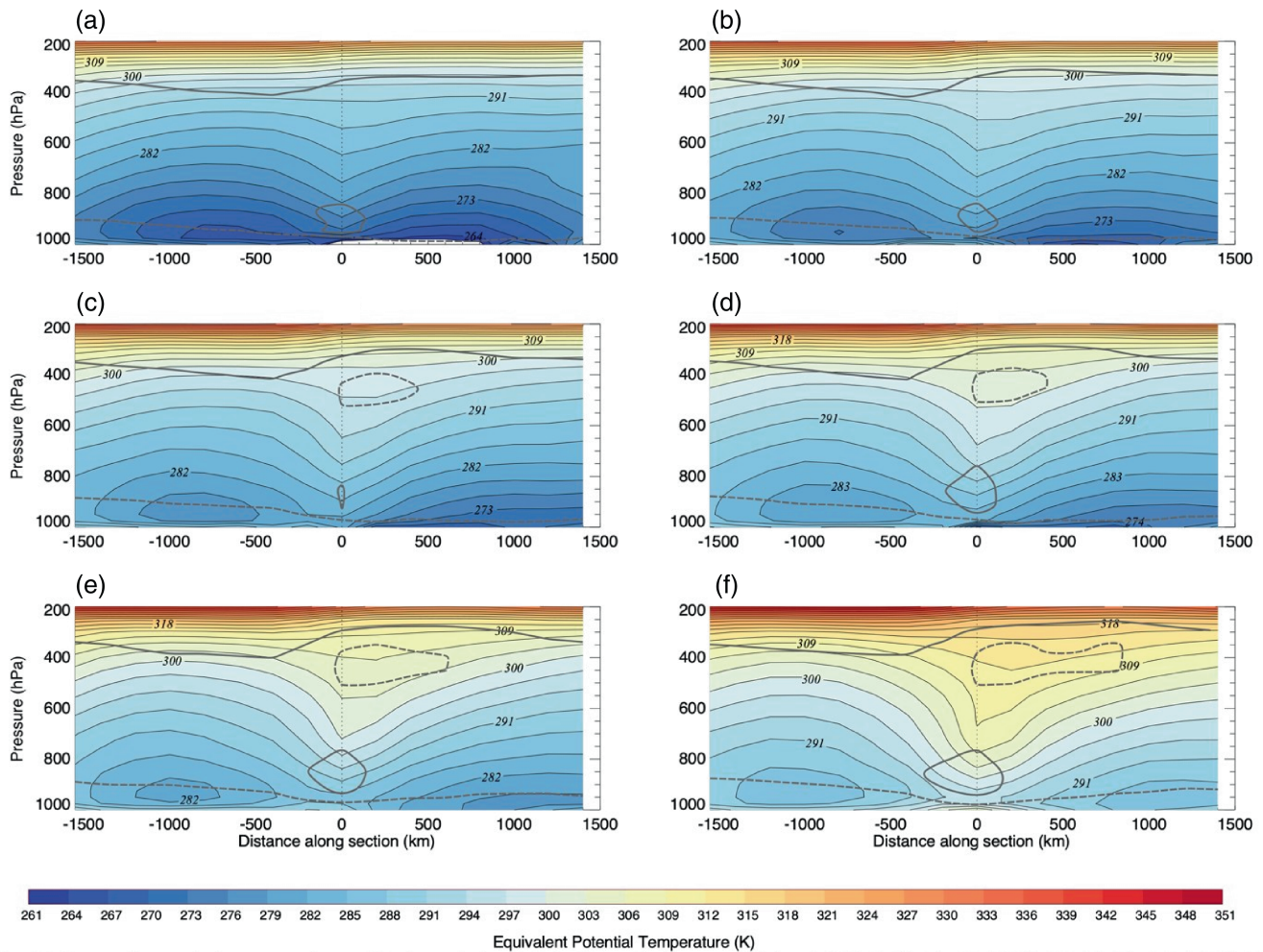


FIGURE 15 Composite vertical cross-sections of θ_e through the occluded thickness ridge (OTR) in Southern-Hemisphere (SH) occlusions comprising (a) Bin I, (b) Bin II, (c) Bin III, (d) Bin IV, (e) Bin V, and (f) Bin VI as identified in Figure 13. Black solid lines are θ_e isentropes labeled in K and contoured and shaded (according to legend) every 3 K. Thick solid (dashed) line is the -1.5 PVU (-0.5 PVU) (potential vorticity units) isertel. Thin dotted line at $x = 0$ in each cross-section identifies the intersection of the composite transect line and the adjusted thermal ridge axis. Distance along the cross-section is indicated in km; positive to poleward and negative for equatorward

of the \vec{Q} Vector (Hoskins *et al.*, 1978), closely related to PVA by the thermal wind (Sutcliffe, 1947; Trenberth, 1978) simultaneously accounts for the production of the OTR and provides the predominant dynamical forcing for ascent in the occluded quadrant of cyclones. The TROWAL air stream, a cyclonically ascending air stream that originates in the warm-sector boundary layer and flows through the TROWAL, is supported by this quasi-geostrophic forcing. The fact that the “warmer” occlusions in the present analysis have both higher θ_e feeding the TROWAL air stream and larger vertical motion within the TROWAL leads them to also produce larger amounts of LHR in the occluded quadrant. Consequently, a couplet of lower-tropospheric cyclonic PV production and upper-tropospheric PV erosion is clearly evident in these composite cross-sections. Additionally, as the maximum 700-hPa θ_e in the TROWAL increases,

so does the robustness of the associated occluded thermal structure (Figures 11 and 15). The coincidence of these structural characteristics in the composites depicted here offers new evidence for the suggestion made by Posselt and Martin (2004) that LHR plays an important role in the production of the canonical occluded thermal structure. The more concentrated and more vigorous composite vertical motions of the NH wintertime occlusions revealed in the analysis remains in need of explanation.

A forthcoming paper will utilize the objective identification scheme illustrated here to construct composites of the cloud structure, microphysics and precipitation characteristics of a global distribution of occlusions based on observations from satellite-based radar and lidar profiles. Also underway is an evaluation of the global distribution of occlusions as portrayed in a free-running integration of

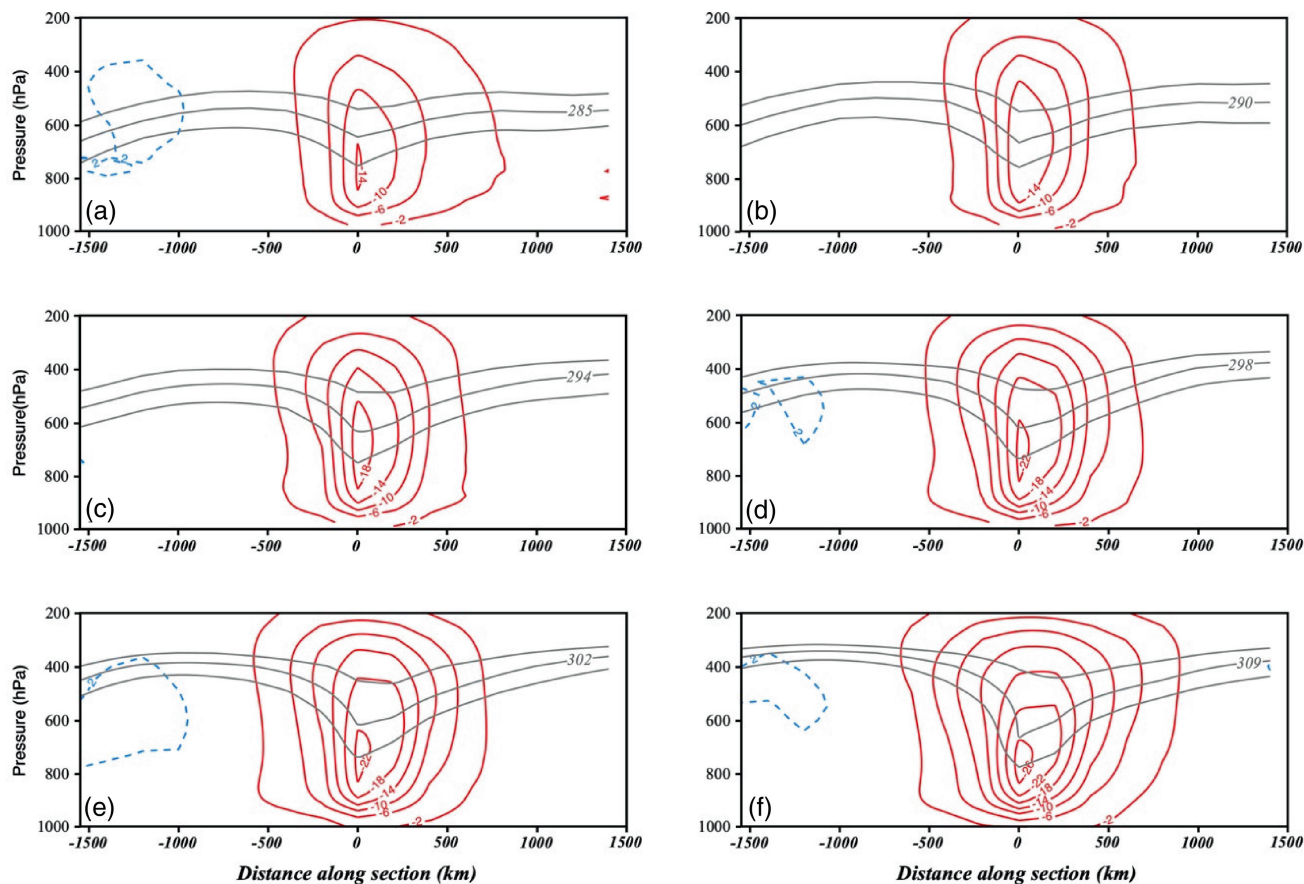


FIGURE 16 Composite vertical motions through the occluded thickness ridge (OTR) in Southern-Hemisphere (SH) occlusions comprising (a) Bin I, (b) Bin II, (c) Bin III, (d) Bin IV, (e) Bin V, and (f) Bin VI as identified in Figure 13. Thin solid red (dashed blue) lines are upward (downward) vertical motion labeled in units of dPa s^{-1} and contoured every 4 dPa s^{-1} starting at -2 (2) dPa s^{-1} . Thicker gray lines in each panel are three consecutive θ_e isentropes from the respective panels in Figure 15, each centered on the isentrope that straddles the 0 point along the x-axis at 700 hPa

different versions of the Goddard Institute for Space Studies Global Climate Model (Kelley *et al.*, 2020). Preliminary results of that analysis suggest that model extratropical cyclones tend to form farther poleward than those in the reanalysis. And though the model does produce occlusions that appear realistic, it does so nearly twice as frequently as the reanalysis. These and other questions regarding the nature of occluded cyclones in a warmer climate can now be considered quantitatively through application of the objective identification method outlined here.

AUTHOR CONTRIBUTIONS

Catherine M. Naud: Data curation; formal analysis; methodology; software; writing – review and editing. **Jonathan E. Martin:** Conceptualization; formal analysis; methodology; validation; writing – original draft; writing – review and editing. **Poushali Ghosh:** Investigation; writing – original draft; writing – review and editing. **Gregory Elsaesser:** Investigation; writing – review and

editing. **Derek Posselt:** Investigation; writing – review and editing.

ACKNOWLEDGEMENTS

The work is funded by NASA's CloudSat-CALIPSO Science Team program grant 80NSSC20K0085. A portion of this research was conducted at the Jet Propulsion Laboratory, California Institute of Technology, under a contract with the National Aeronautics and Space Administration (80NM0018D0004). The authors thank one anonymous reviewer and David Schultz for their insightful comments that helped improve this manuscript.

DATA AVAILABILITY STATEMENT

The database of cyclone locations is available at <https://portal.nccs.nasa.gov/datashare/Obs-ETC/>. MERRA-2 files used in the analysis are: Global Modeling and Assimilation Office (GMAO) (2015), MERRA-2 inst3_3d_asm_Np: 3d, 3-Hourly, Instantaneous, Pressure-Level, Assimilation, Assimilated Meteorological


Fields V5.12.4, Greenbelt, MD, USA, Goddard Earth Sciences Data and Information Services Center (GES DISC), Accessed: 2020-01, 10.5067/QBZ6MG944HW0, Global Modeling and Assimilation Office (GMAO) (2015), MERRA-2 inst6_3d_ana_Np: 3d, 6-Hourly, Instantaneous, Pressure-Level, Analysis, Analyzed Meteorological Fields V5.12.4, Greenbelt, MD, USA, Goddard Earth Sciences Data and Information Services Center (GES DISC), Accessed: 2020-01, 10.5067/A7S6XP56VZWS.

ORCID

Catherine M. Naud  <https://orcid.org/0000-0002-3914-1498>

Jonathan E. Martin  <https://orcid.org/0000-0003-3992-8458>

Poushali Ghosh  <https://orcid.org/0000-0002-3319-0416>

Gregory Elsaesser  <https://orcid.org/0000-0001-5785-4451>

Derek Posselt  <https://orcid.org/0000-0002-5670-5822>

REFERENCES

- Atkinson, B.W. and Smithson, P.A. (1974) Meso-scale circulations and rainfall patterns in an occluding depression. *Quarterly Journal of the Royal Meteorological Society*, 100(423), 3–22.
- Bauer, M. and Del Genio, A.D. (2006) Composite analysis of winter cyclones in a GCM: influence on climatological humidity. *Journal of Climate*, 19(9), 1652–1672.
- Bauer, M., Tselioudis, G. and Rossow, W.B. (2016) A new climatology for investigating storm influences in and on the extratropics. *Journal of Applied Meteorology and Climatology*, 55(5), 1287–1303. <https://doi.org/10.1175/JAMC-D-15-0245.1>.
- Berman, J.D. and Torn, R.D. (2019) The impact of initial condition and warm conveyor belt forecast uncertainty on variability in the downstream waveguide in an ECWMF case study. *Monthly Weather Review*, 147(11), 4071–4089.
- Berry, G., Jakob, C. and Reeder, M. (2011) Recent global trends in atmospheric fronts. *Geophysical Research Letters*, 38(21), L21812, 1–6.
- Bjerknes, J. and Solberg, H. (1922) Life cycle of cyclones and the polar front theory of atmospheric circulation. *Geophysiska Publikationer*, 3(1), 1–18.
- Browning, K.A. (1990) Organization of clouds and precipitation in extratropical cyclones. In: Newton, C.W. and Holopainen, E.O. (Eds.) *Extratropical Cyclones: The Erik Palmén Memorial Volume*. Boston, MA: American Meteorological Society, pp. 129–153.
- Browning, K.A. and Harrold, T.W. (1969) Air motion and precipitation growth in a wave depression. *Quarterly Journal of the Royal Meteorological Society*, 95, 288–309.
- Carlson, T.N. (1980) Airflow through midlatitude cyclones and the comma cloud pattern. *Monthly Weather Review*, 108, 1498–1509.
- Crocker, A., Godson, W.L. and Penner, C.M. (1947) Frontal contour charts. *Journal of the Atmospheric Sciences*, 4(3), 95–99.
- Dee, D.P., Uppala, S.M., Simmons, A.J., Berrisford, P., Poli, P., Kobayashi, S., Andrae, U., Balmaseda, M.A., Balsamo, G., Bauer, D.P. and Bechtold, P. (2011) The ERA-interim reanalysis: configuration and performance of the data assimilation system. *Quarterly Journal of the Royal Meteorological Society*, 137(656), 553–597.
- Eckhardt, S., Stohl, A., Wernli, H., James, P., Forster, C. and Spichtinger, N. (2004) A15-year climatology of warm conveyor belts. *Journal of Climate*, 17, 218–237.
- Eliassen, A. and Kleinschmidt, E. (1957) *Dynamic Meteorology*. Berlin Heidelberg: Springer, pp. 1–154.
- Galloway, J.L. (1958) The three-front model: its philosophy, nature, construction and use. *Weather*, 13(1), 3–10.
- Galloway, J.L. (1960) The three-front model, the developing depression and the occluding process. *Weather*, 15(9), 293–309.
- Gelaro, R., McCarty, W., Suarez, M.J., Todling, R., Molod, A., Takacs, L., et al. (2017) The modern-era retrospective analysis for research and applications, version 2 (MERRA-2). *Journal of Climate*, 30(14), 5419–5454.
- Godson, W.L. (1951) Synoptic properties of frontal surfaces. *Quarterly Journal of the Royal Meteorological Society*, 77(334), 633–653.
- Harrold, T.W. (1973) Mechanisms influencing the distribution of precipitation within baroclinic disturbances. *Quarterly Journal of the Royal Meteorological Society*, 99, 232–251.
- Hewson, T.D. (1998) Objective fronts. *Meteorological Applications*, 5(1), 37–65.
- Hewson, T.D. and Titley, H.A. (2010) Objective identification, typing and tracking of the complete life-cycles of cyclonic features at high spatial resolution. *Meteorological Applications*, 17(3), 355–381.
- Hoskins, B.J. (1999) Sutcliffe and his development theory. In: Shapiro, M.A. and Grønås, S. (Eds.) *The Life Cycles of Extratropical Cyclones*. Boston, MA: American Meteorological Society, pp. 81–86. https://doi.org/10.1007/978-1-935704-09-6_8
- Hoskins, B.J., Draghici, I. and Davies, H. (1978) A new look at the ω -equation. *Quarterly Journal of the Royal Meteorological Society*, 104(439), 31–38.
- Hoskins, B.J. and Hodges, K.I. (2005) A new perspective on southern hemisphere storm tracks. *Journal of Climate*, 18(20), 4108–4129.
- Hoskins, B.J., McIntyre, M.E. and Robertson, A.W. (1985) On the use and significance of isentropic potential vorticity maps. *Quarterly Journal of the Royal Meteorological Society*, 111(470), 877–946.
- Iskenderian, H. (1988) Three-dimensional airflow and precipitation structure in a nondeepening cyclone. *Weather and Forecasting*, 3(1), 18–32.
- Jewell, R. (1981) Tor Bergeron's first year in the Bergen school: towards an historical appreciation. In: Lilequist, G.H. (Ed.) *Weather and Weather Maps: A Volume Dedicated to the Memory of Tor Bergeron. Vol. 10, Contributions to Current Research in Geophysics*. Springer, pp. 474–490.
- Kalnay, E., Kanamitsu, M., Kistler, R., Collins, W., Deaven, D., Gandin, L., Iredell, M., Saha, S., White, G., Woollen, J. and Zhu, Y. (1996) The NCEP/NCAR 40-year reanalysis project. *Bulletin of the American Meteorological Society*, 77(3), 437–472.
- Kelley, M., Schmidt, G.A., Nazarenko, L.S., Bauer, S.E., Ruedy, R., Russell, G.L., Ackerman, A.S., Aleinov, I., Bauer, M., Bleck, R. and Canuto, V. (2020) GISS-e2. 1: configurations and climatology. *Journal of Advances in Modeling Earth Systems*, 12(8), e2019MS002025.
- Keyser, D., Schmidt, B.D. and Duffy, D.G. (1992) Quasigeostrophic vertical motions diagnosed from along-and cross-isentropic components of the Q vector. *Monthly Weather Review*, 120(5), 731–741.

- Kurz, M. (1988) Development of cloud distribution and relative motions during the mature and occlusion stage of a typical cyclone development. Preprints. In: *Palmen Memorial Symp. on Extratropical Cyclones, Helsinki, Finland*. Boston, MA: American Meteorological Society, pp. 201–204.
- Madonna, E., Wernli, H., Joos, H. and Martius, O. (2014) Warm conveyor belts in the ERA-interim dataset (1979–2010). Part I: climatology and potential vorticity evolution. *Journal of Climate*, 27, 3–26. <https://doi.org/10.1175/JCLI-D-12-00720.1>.
- Martin, J.E. (1998a) The structure and evolution of a continental winter cyclone. Part I: frontal structure and the occlusion process. *Monthly weather review*, 126(2), 303–328.
- Martin, J.E. (1998b) The structure and evolution of a continental winter cyclone. Part II: frontal forcing of an extreme snow event. *Monthly weather review*, 126(2), 329–348.
- Martin, J.E. (1999a) Quasi-geostrophic forcing of ascent in the occluded sector of cyclones and the trowal airstream. *Monthly weather review*, 127, 70–88.
- Martin, J.E. (1999b) The separate roles of geostrophic vorticity and deformation in the mid-latitude occlusion process. *Monthly weather review*, 127, 2404–2418.
- Martin, J.E. (2006) *Mid-Latitude Atmospheric Dynamics: A First Course*. West Sussex, England: John Wiley Sons, Ltd.
- Martínez-Alvarado, O., Joos, H., Chagnon, J., Boettcher, M., Gray, S.L., Plant, R.S., et al. (2014) The dichotomous structure of the warm conveyor belt. *Quarterly Journal of the Royal Meteorological Society*, 140(683), 1809–1824.
- Mass, C.F. and Schultz, D.M. (1993) The structure and evolution of a simulated midlatitude cyclone over land. *Monthly weather review*, 121, 889–917.
- Namias, J. (1939) The use of isentropic analysis in short term forecasting. *Journal of the aeronautical sciences*, 6(7), 295–298.
- Naud, C.M., Posselt, D.J. and van den Heever, S.C. (2012) Observational analysis of cloud and precipitation in midlatitude cyclones: northern versus southern hemisphere warm fronts. *Journal of Climate*, 25(14), 5135–5151.
- Naud, C.M., Posselt, D.J. and van den Heever, S.C. (2015) A CloudSat–CALIPSO view of cloud and precipitation properties across cold fronts over the global oceans. *Journal of Climate*, 28, 6743–6762.
- Naud, C.M., Posselt, D.J. and van den Heever, S.C. (2018) Reply to comments on ‘A CloudSat–CALIPSO view of cloud and precipitation properties across cold fronts over the global oceans’. *Journal of Climate*, 31(7), 2969–2975. <https://doi.org/10.1175/JCLI-D-17-0777.1>.
- Penner, C. (1955) A three-front model for synoptic analyses. *Quarterly Journal of the Royal Meteorological Society*, 81(347), 89–91.
- Polly, J.B. and Rossow, W.B. (2016) Cloud radiative effects and precipitation in extratropical cyclones. *Journal of Climate*, 29(18), 6483–6507.
- Posselt, D.J. and Martin, J.E. (2004) The effect of latent heat release on the evolution of a warm occluded thermal structure. *Monthly weather review*, 132(2), 578–599.
- Raymond, D. (1992) Nonlinear balance and potential-vorticity thinking at large Rossby number. *Quarterly Journal of the Royal Meteorological Society*, 118(507), 987–1015.
- Reed, R.J., Kuo, Y.-H. and Low-Nam, S. (1994) An adiabatic simulation of the erica iop 4 storm: an example of quasi-ideal frontal cyclone development. *Monthly Weather Review*, 122(12), 2688–2708.
- Saha, S., Moorthi, S., Pan, H.L., Wu, X., Wang, J., Nadiga, S., Tripp, P., Kistler, R., Woollen, J., Behringer, D. and Liu, H. (2010) The NCEP climate forecast system reanalysis. *BAMS*, 91(8), 1015–1058.
- Saucier, W.J. (1955) *Principles of Meteorological Analysis*, Vol. 438. Chicago, Ill: University of Chicago Press.
- Schäfler, A. and Harnisch, F. (2015) Impact of the inflow moisture on the evolution of a warm conveyor belt. *Quarterly Journal of the Royal Meteorological Society*, 141(686), 299–310.
- Schemm, S., Sprenger, M. and Wernli, H. (2018) When during their life cycle are extratropical cyclones attended by fronts? *Bulletin of the American Meteorological Society*, 99(1), 149–165.
- Schultz, D.M. (2018) Comments on “a CloudSat–CALIPSO view of cloud and precipitation properties across cold fronts over the global oceans.”. *Journal of Climate*, 31, 2965–2967. <https://doi.org/10.1175/JCLI-D-17-0619.1>.
- Schultz, D.M. and Mass, C.F. (1993) The occlusion process in a midlatitude cyclone over land. *Monthly weather review*, 121(4), 918–940.
- Schultz, D.M. and Vaughan, G. (2011) Occluded fronts and the occlusion process: a fresh look at conventional wisdom. *Bulletin of the American Meteorological Society*, 92(4), 443–466.
- Simmonds, I., Keay, K. and Tristram Bye, J.A. (2012) Identification and climatology of southern hemisphere mobile fronts in a modern reanalysis. *Journal of Climate*, 25(6), 1945–1962.
- Stephens, G.L., Vane, D.G., Boain, R.J., Mace, G.G., Sassen, K., Wang, Z., Illingworth, A.J., O’Connor, E.J., Rossow, W.B., Durden, S.L., Miller, S.D., Austin, R.T., Benedetti, A., Mitrescu, C. and CloudSat Science Team, 2002. (2002) The CloudSat mission and the A-train: a new dimension of space-based observations of clouds and precipitation. *Bulletin of the American Meteorological Society*, 83(12), 1771–1790.
- Stoelinga, M.T., Locatelli, J.D. and Hobbs, P.V. (2002) Warm occlusions, cold occlusions, and forward-tilting cold fronts. *Bulletin of the American Meteorological Society*, 83(5), 709–722.
- Sutcliffe, R. (1947) A contribution to the problem of development. *Quarterly Journal of the Royal Meteorological Society*, 73(317–318), 370–383.
- Thomas, C.M. and Schultz, D.M. (2019a) Global climatologies of fronts, air mass boundaries, and airstream boundaries: why the definition of “front” matters. *Monthly Weather Review*, 147, 691–717. <https://doi.org/10.1175/MWR-D-18-0289.1>.
- Thomas, C.M. and Schultz, D.M. (2019b) What are the best thermodynamic quantity and function to define a front in gridded model output? *Bulletin of the American Meteorological Society*, 100, 873–895. <https://doi.org/10.1175/BAMS-D-18-0137.1>.
- Trenberth, K.E. (1978) On the interpretation of the diagnostic quasi-geostrophic omega equation. *Monthly Weather Review*, 106(1), 131–137.
- Wallace, J.M. and Hobbs, P. (1977) *Atmosphere science-an introductory survey*. V, V.
- Wernli, H. (1997) A Lagrangian-based analysis of extratropical cyclones. II: a detailed case-study. *Quarterly Journal of the Royal Meteorological Society*, 23, 1677–1706.
- Wernli, H. and Davies, H.C. (1997) A Lagrangian-based analysis of extratropical cyclones. I: the method and some applications.

Quarterly Journal of the Royal Meteorological Society, 123(538), 467–489.

Winker, D.M., Vaughan, M.A., Omar, A., Hu, Y., Powell, K.A., Liu, Z., Hunt, W.H. and Young, S.A. (2009) Overview of the CALIPSO mission and CALIOP data processing algorithms. *Journal of Atmospheric and Oceanic Technology*, 26(11), 2310–2323.

Young, M.V., Monk, G.A. and Browning, K.A. (1987) Interpretation of satellite imagery of a rapidly deepening cyclone. *Quarterly Journal of the Royal Meteorological Society*, 113(478), 1089–1115.

How to cite this article: Naud, C.M., Martin, J.E., Ghosh, P., Elsaesser, G. & Posselt, D. (2023) Automated identification of occluded sectors in midlatitude cyclones: Method and some climatological applications. *Quarterly Journal of the Royal Meteorological Society*, 149(754), 1990–2010. Available from: <https://doi.org/10.1002/qj.4491>